The Astrophysical Journal, 844:62 (35pp), 2017 July 20 https://doi.org/10.3847/1538-4357/aa78f4

Long-term Study of the Light Curve of PKS 1510-089 in GeV Energies

Raj Prince[1], Pratik Majumdar[2], and Nayantara Gupta[1]
[1] Raman Research Institute, Sadashivanagar, Bangalore 560080, India; rajprince@rri.res.in
[2] Saha Institute of Nuclear Physics, HBNI, Kolkata, West Bengal 700064, India
Received 2017 February 22; revised 2017 June 3; accepted 2017 June 6; published 2017 July 21

Abstract

We have analyzed data from the flat-spectrum radio quasar PKS 1510-089 collected over a period of eight years from 2008 August to 2016 December with the *Fermi*-LAT. We have identified several flares of this highly variable source, studied their temporal and spectral properties in detail, and compared with previous works on flares of PKS 1510-089. Five major flares and a few subflares or substructures have been identified in our study. The fastest variability time is found to be 1.30 ± 0.18 hr between MJD 55852.063 and 55852.188, where we estimate the minimum size of the emission region to be 4.85×10^{15} cm. In most of the flares, the spectral energy distributions are better fitted with a log-parabolic distribution compared to a simple power law or a power law with exponential cutoffs. This has strong physics implications regarding the nature of the high-energy gamma-ray emission region.

Key words: galaxies: active – gamma rays: galaxies – quasars: individual (PKS 1510-089)

Supporting material: data behind figure

1. Introduction

Understanding the physics of blazar flares is one of the most intriguing topics of research in high-energy gamma-ray astronomy. The origin of flux variability or flares could be in internal shocks in the blazar jets, as discussed in earlier studies (Spada et al. 2001). It could also be from perturbation in the accretion rate, variations in activity of the central engine (Kelly et al. 2011), or fluctuations in the local magnetic field and particle densities. The observed emissions of different frequencies could be from a single zone or multiple zones. Depending on the spectral properties of the sources, the underlying mechanism of variable emission may vary from one source to another.

PKS 1510-089, located at a redshift of 0.361 (Burbidge & Kinman 1966; Thompson et al. 1990), is highly variable and has been observed in gamma-ray energies up to 400 GeV (Abramowski et al. 2013, HESS Collaboration; Aleksić et al. 2014, MAGIC Collaboration). This highly variable flat-spectrum radio quasar (FSRQ) has been monitored by *Fermi*-LAT over a period of eight years (2008–2016). The multiwavelength data from flares of PKS 1510-089 during its high state between 2008 September and 2009 June showed variabilities in timescales of 6–12 hr (Abdo et al. 2010a, *Fermi*-LAT Collaboration). The *Fermi*-LAT collaboration recorded isotropic luminosity in gamma rays of approximately 2×10^{48} erg s^{-1} on 2009 March 26. This luminosity exceeds the estimated Eddington's luminosity $L_{\rm Edd} = 6.86 \times 10^{46}$ erg s^{-1}. This is calculated by using the black hole mass given in Abdo et al. (2010a). It is hard to find correlations in emissions in different frequencies (Ahnen et al. 2017, MAGIC Collaboration).

The multiwavelength emission of PKS 1510-089 has been modeled previously in the framework of both leptonic and hadronic models.

In the leptonic model, the low-energy component of the spectral energy distribution (SED) is produced by synchrotron radiation of relativistic electrons in the jet. The high-energy component is produced by the inverse Compton (IC) process, where the seed photons can be due to synchrotron radiation (commonly called the synchrotron self Compton process) or photons from the broad line region (BLR) or dusty torus (DT; commonly known as the external Compton radiation, or EC). For more details on EC modeling, see Barnacka et al. (2014), Aleksić et al. (2014), Böttcher & Dermer (1998), and Tavecchio & Ghisellini (2008).

In hadronic models, the required jet luminosity is high (Böttcher et al. 2013) because proton cooling is much more inefficient than electron cooling. A proton synchrotron origin of X-ray and gamma-ray emission has been considered recently (Pratim Basumallick & Gupta 2017) to explain the week-scale flares (during 2009 March–April and 2012 February–April) of PKS 1510-089. In this study, they have fitted the radio to gamma-ray data with a single-zone model of synchrotron emission from electrons and protons for a jet luminosity comparable to Böttcher et al. (2013).

The study of the light curve and the identification of the location of the flares (Tavecchio et al. 2010) are of much interest due to the wealth of flare data observed by *Fermi*-LAT. It has been suggested before that there could be multiple simultaneously active gamma-ray emission regions along the jet of PKS 1510-089 (Brown 2013). Dotson et al. (2012) discussed locating the distances of the emission regions of flares from the black hole with the cooling timescales of the energetic electrons. The temperature and density of the seed photons are different in the BLR and molecular torus (MT) regions, which determine the IC cooling regime (Klein–Nishina or Thomson) and timescale of the electrons. The maximum decay time difference of the flares could impose an upper limit on the location of the flares. For the luminosity of seed photons in the MT region of 10^{45} erg s^{-1} and the Lorentz factor of the jet $\Gamma = 10$, they found the distance of the flare to be within 2.3×10^{18} cm for the *Fermi*-LAT observed flares of energy between 100 MeV to 1 GeV. In a more recent study, Dotson et al. (2015) have discussed that the emission regions of the 2009 GeV flares of PKS 1510-089 are distributed over a large distance along the length of the jet ranging from the

BLR to the MT and to the VLBI radio core zone 10 pc away from the black hole.

Due to the extreme variability of the source, the light curve of PKS 1510-089 has shown many interesting results and has been studied by various authors (Abdo et al. 2010a; Foschini et al. 2013; Ahnen et al. 2017; Zacharias et al. 2016). However, most of the work that can be found in the literature has been focused on the variability studies on short timescales (of a few hours to a few tens of minutes). As of now, not much effort has been concentrated on studying the long-term light curve of the source. In this paper, we aim to address the long-term light curve of PKS 1510-089 in the gamma-ray band using the data collected over a period of eight years with the *Fermi*-LAT detector.

From the *Fermi*-LAT data collected over a period of eight years, we have selected the high states or flares of PKS 1510-089 to compare their spectral and temporal properties. Although some of these high states of PKS 1510-089 have been studied before by other authors, a comprehensive study including all of the high states observed by the *Fermi*-LAT Collaboration up to 2016 December and a comparison of their spectral and temporal characteristics is not available in the literature. Thus our work provides a detailed, complete, and updated analysis of the flares of PKS 1510-089 detected by *Fermi*-LAT. The rest of the paper is organized as follows. In Section 2, we describe the data analysis procedures, conduct a detailed study of various flares, and construct the SEDs of the various states of the source. In Section 3 we discuss the results and draw conclusions from our analysis.

Throughout the paper we note the flux in units of 10^{-6} ph cm^{-2} s^{-1} unless otherwise mentioned.

2. *Fermi*-LAT Data Analysis of PKS 1510-089

The *Fermi*-LAT is a pair-conversion γ-ray telescope sensitive to photon energies greater than 20 MeV with a field of view of about 2.4 sr (Atwood et al. 2009). The primary observation mode of *Fermi*-LAT is survey mode in which the LAT (Large Area Telescope) scans the entire sky every 3 hr. PKS 1510-089 has been continuously monitored by *Fermi*-LAT since 2008 August. We consider here the *Fermi*-LAT data for PKS 1510-089 from 2008 August 05 to 2016 December 31 (MJD 54683–57753). The data analysis has been done with the help of the *gtlike/pyLikelihood* method, as implemented in the latest version (v10r0p5) of the *Fermi Science Tools* software package. In this analysis, we have considered photons of energy greater than 100 MeV.

Gamma (γ) rays are also produced in the upper atmosphere by the interaction of cosmic rays with ambient medium matter or radiation. In order to reduce the contribution from these γ rays (also called Earth limb γ rays), our analysis is restricted to a maximum zenith angle of 105°. The latest *Fermi Science Tools* include the instrument response function (IRF) "P8R2_SOURCE_V6," which has been used in the analysis. The photons are extracted from a circular region of 10° around the source, which is also called the region of interest (ROI). To include all of the sources lying within the ROI, we have used the third *Fermi*-LAT catalog (3FGL; Acero et al. 2015). The spectral parameters were left free for sources lying within the 10°. It must be noted that several other sources are also present in the 10°–20° ROI. In the model file, their spectral parameters have been kept fixed to the 3FGL catalog value. To gauge the significance of the γ-ray signal, we have done the maximum likelihood (ML) test, which is defined by TS $= 2\Delta$ log(L), where L is the likelihood function between models with and without a point source at the position of the source of interest (Paliya 2015). We have first performed the ML analysis over the period of interest, and for further analysis we have removed the sources of TS < 9 (TS $= 9$ corresponds to $\sim 3\sigma$ detection; for details see Mattox et al. 1996). The standard background model was used to extract the spectral information. In our analysis, we have also used the latest isotropic background model, "iso_P8R2_SOURCE_V6_v06," and the Galactic diffuse emission model "gll_iem_v06" (available on the *Fermi Science Tools* website[3]). The variability of the source can be clearly seen by producing light curves with different time bins (7 days, 1 day, 12 hr, 6 hr, and 3 hr). In Figure 1, we show the weekly light curve, which clearly reveals that the source is highly variable. In addition, we performed the spectral analysis in the energy range 0.1–300 GeV over several periods of the flaring states by using the *unbinned likelihood analysis*.

The differential photon spectra have been fitted with three different functions, whose forms are presented below:

1. A power law (PL), defined as

$$dN(E)/dE = N_p(E/E_p)^{-\Gamma}, \quad (1)$$

with $E_p = 100$ MeV (constant for all of the SEDs).

2. A log parabola (LP), defined as

$$dN(E)/dE = N_0(E/E_0)^{-\alpha-\beta\ln(E/E_0)}, \quad (2)$$

with $E_0 = 300$ MeV (constant for all of the SEDs), where α is the photon index at E_0, β is the curvature index, and "ln" is the natural logarithm.

3. A power law with an exponential cutoff (PLEC), defined as

$$dN(E)/dE = N_0(E/E_p)^{-\Gamma}\exp(-E/E_c), \quad (3)$$

with $E_p = 200$ MeV (constant for all of the SEDs).

2.1. Identifying the Flares of PKS 1510-089

PKS 1510-089 is one of the most variable (variability index = 11014.00) blazars in the 3FGL catalog. The variability can be seen in Figure 1, which shows the weekly light curve history of the source observed by the *Fermi*-LAT during 2008 August to 2016 December. Most of the time, PKS 1510-089 is in a quiescent state, accompanied by occasional periods of high activity where the flux greatly surpasses the quiescent-state flux. These episodes of high activity are also referred to as flaring states. The duration of the flaring state is very short (ranging from a few days to a couple of weeks), after which the source returns to its pre-flare quiescent state.

[3] https://fermi.gsfc.nasa.gov/ssc/data/access/lat/BackgroundModels.html

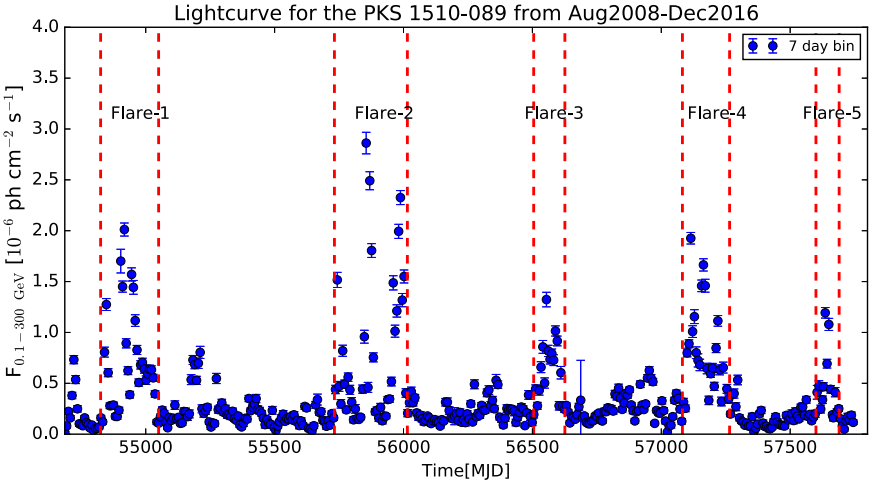

Figure 1. Light curve history of PKS 1510-089. Five flare episodes have been identified and further studied. Their time durations are as follows: MJD 54825–55050, MJD 55732–56015, MJD 56505–56626, MJD 57082–57265, and MJD 57657–57753, which are shown by dashed red lines. The data used to create this figure are available.

The light curve history of PKS 1510-089 shows that so far there have been five major flaring states (see Figure 1). We refer to these states in our work as Flare-1, Flare-2, Flare-3, Flare-4, and Flare-5, which happened during MJD 54825–55050, MJD 55732–56015, MJD 56505–56626, MJD 57082–57265, and MJD 57657–57753, respectively. We have zoomed out these major flares in bins of 1 day (not shown here), where substructures are not clearly seen, 6 hr (primarily for the light curve study), and 3 hr (for the variability timescale study). The 6 hr binning clearly reveals that there are substructures and various phases (pre-flare, plateau, flare, and post-flare) inside each individual flare shown in Figure 1. For further study, we concentrate on the plots with 6 hr bins. Two substructures have been observed during Flare-1: we label them as flare-1(A) and flare-1(B). Flare-2 shows five substructures defined as flare-2(A), 2(B), 2(C), 2(D), and 2(E). No substructure was seen during Flare-3 and Flare-5, while three substructures were noticed during Flare-4 and are defined as flare-4(A), 4(B), and 4(C). All the different phases of activity have been marked with vertical dashed red lines (see Figures 2–13). The time intervals that have TS < 9 are rejected from the light curve analysis.

2.2. Light Curves of Flares

As seen from Figure 1, we can clearly make out five major flaring episodes of PKS 1510-089. We have studied the temporal evolution of each flare separately. In order to show the temporal evolution, we have fitted the peaks by a sum of exponentials that give the decay and rising time for the different peaks shown in the light curve plots. The quiescent state (designated by the light gray line in the figures) is also presented in the light curve plots with the peaks of the flaring states. The functional form of the sum of exponentials is

$$F(t) = 2F_0\left[\exp\left(\frac{t_0 - t}{T_r}\right) + \exp\left(\frac{t - t_0}{T_d}\right)\right]^{-1} \quad (4)$$

(Abdo et al. 2010b), where F_0 is the flux at time t_0 representing the approximate flare amplitude, and T_r and T_d are the rise and decay times of the flare.

2.2.1. Flare-1

Figures 2 and 3 show the light curves of flare-1(A) and flare-1(B) in time bins of 6 hr corresponding to the flaring activity during MJD 54890–54927 and MJD 54935–54965, respectively.

In Figure 2 there are no *Fermi*-LAT data available in the time range MJD 54901.2–54905.6, and before 54899.0 the source was in a quiescent state. We define this quiescent state as the pre-flare epoch of the source. The flaring activity in flare-1(A) can be further divided into two parts: flare(I) and flare(II). The flare(I) phase was observed during MJD 54899.0 to 54910.3, where it shows two peaks P1 and P2 around MJD 54906.4 and 54909.1 with flux $F_{\rm GeV} = 2.34 \pm 0.40$ and 2.92 ± 0.45, respectively. After this, the source resides in a state where the flux exceeds the constant value of 0.64 ± 0.07 for almost five days (MJD 54910.3-54915.0). This particular state, which is neither the quiescent state nor a fully fledged flaring state, is referred to as the "plateau." After spending a few days in the so-called plateau state (average flux $= 1.38 \pm 0.06$), the flux rises again (flare(II)) and shows one major peak P3 at 54916.9 with a flux of $F_{\rm GeV} = 5.73 \pm 0.50$. A post-flare phase was also observed during MJD 54921 to 54927 with a flux almost close to that of the quiescent state. The decay and rising times of the peaks are tabulated in Table 1.

A pre-flare was also observed during flare-1(B) (see Figure 3), whose flux of $F_{\rm GeV} = 0.61 \pm 0.04$ (during time period MJD 54935 to 54944) is in close proximity to that of the quiescent state.

The flaring phase started from MJD $\sim$ 54944 and persisted for about seven days, reaching a maximum flux of $F_{\rm GeV} = 4.49 \pm 0.52$ around MJD 54947.9 (P2). The peak P1 was observed at MJD 54947.4 with a flux of $F_{\rm GeV} = 3.85 \pm 0.55$. The peak P2 is followed by two peaks P3 and P4 at MJD 54948.6 and 54949.6 with flux of $F_{\rm GeV} = 3.25 \pm 0.39$ and 3.31 ± 0.40, respectively. Two post-flares were also observed in the vicinity of the quiescent state. However, we did not consider them within the flare region as the amplitude of the first one is much lower than the other peaks in the flaring state and the second one is far away from

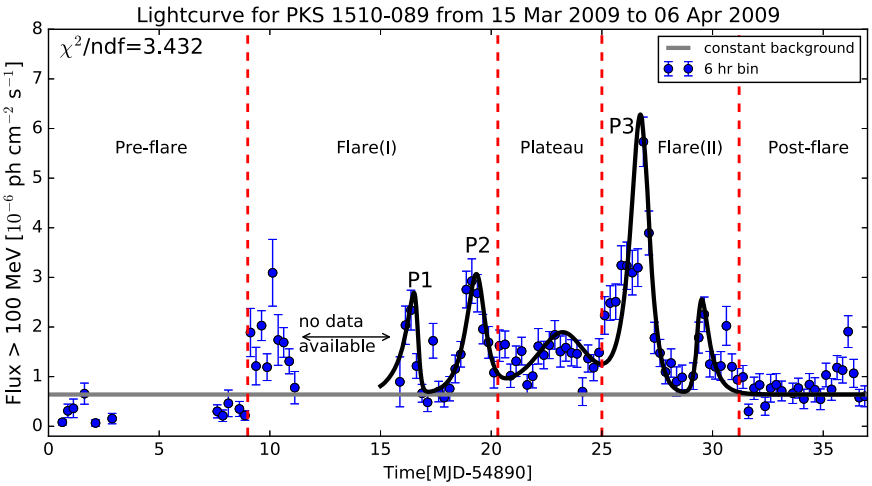

Figure 2. Light curve for flare-1(A) fitted by the sum of exponentials (see the text for details). The fitted parameters are given in Table 1. All of the different periods of activity have been separated by dashed red lines, and the light gray line represents the constant state or flux.

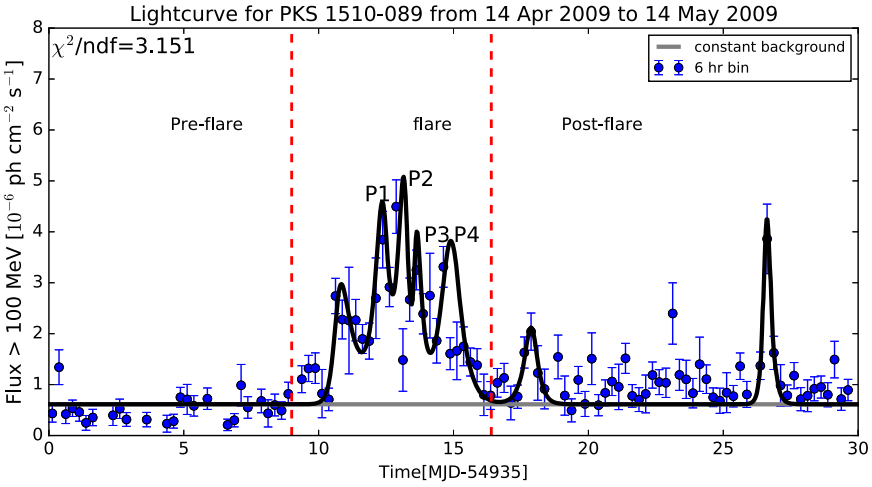

Figure 3. Light curve for flare-1(B) fitted by the sum of exponentials (see the text for details). The fitted parameters are given in Table 1. All of the different periods of activity have been separated by dashed red lines, and the light gray line represents the constant state or flux.

Table 1
Results of Temporal Fitting with Sum of Exponentials (Equation (4) in the Text) for Different Peaks of Flare-1

Peak	t_0 (MJD)	F_0 (10^{-6} ph cm^{-2} s^{-1})	T_r (hr)	T_d (hr)
		flare-1(A)		
P1	54906.4	2.34 ± 0.40	13.76 ± 7.30	2.06 ± 1.27
P2	54909.1	2.92 ± 0.45	10.97 ± 2.32	7.26 ± 2.25
P3	54916.9	5.73 ± 0.50	10.56 ± 1.58	7.75 ± 0.98
		flare-1(B)		
P1	54947.4	3.85 ± 0.55	6.43 ± 2.66	4.04 ± 2.52
P2	54947.9	4.49 ± 0.52	5.71 ± 2.73	2.99 ± 1.23
P3	54948.6	3.25 ± 0.39	1.93 ± 1.98	4.83 ± 2.08
P4	54949.6	3.31 ± 0.40	7.86 ± 2.55	7.85 ± 1.64

Note. Column 2 represents the time (in MJD) at which the peaks are observed, and the peak fluxes are given in column 3. The fitted rise (T_r) and decay (T_d) times are listed in columns 4 and 5.

the main flaring phase. However, it should be noted that the χ^2 of the fit improves significantly if these additional small flares are included in the fit. A few outliers were also observed during this epoch for a very short time period (6 hr). The decay and rising times for the peaks are mentioned in Table 1.

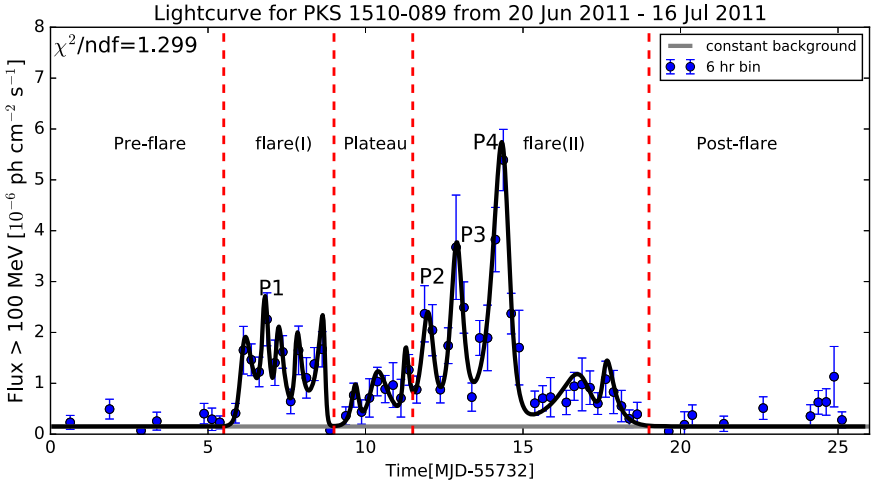

Figure 4. Light curve for flare-2(A) fitted by the sum of exponentials (see the text for details). The fitted parameters are given in Table 2. All of the different periods of activity have been separated by dashed red lines, and the light gray line represents the constant state or flux.

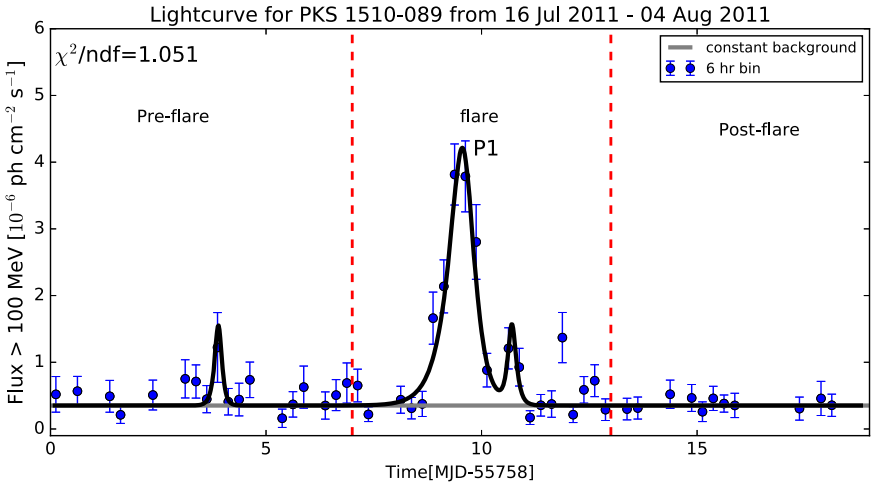

Figure 5. Light curve for flare-2(B) fitted by the sum of exponentials (see the text for details). The fitted parameters are given in Table 2. All of the different periods of activity have been separated by dashed red lines, and the light gray line represents the constant state or flux.

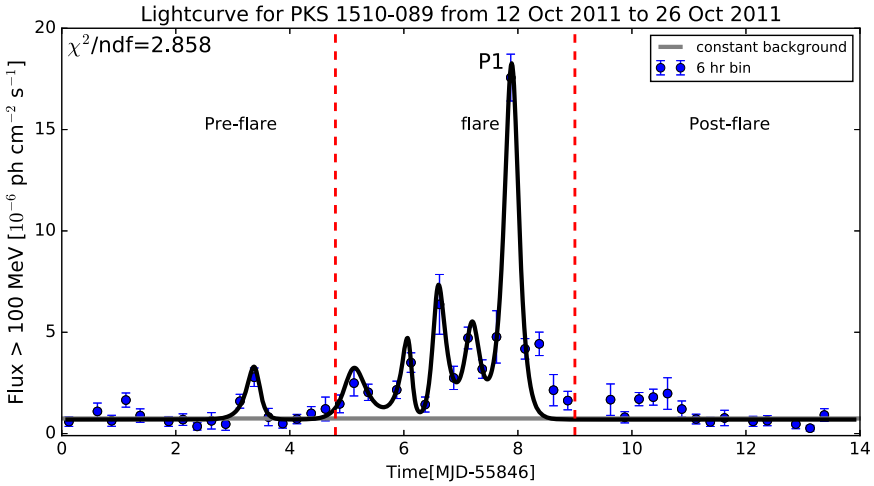

Figure 6. Light curve for flare-2(C) fitted by the sum of exponentials (see the text for details). The fitted parameters are given in Table 2. All of the different periods of activity have been separated by dashed red lines, and the light gray line represents the constant state or flux.

2.2.2. Flare-2

Similar to Flare-1, we carried out the 6 hr binning of Flare-2 (MJD 55732–56015), which shows the various substructures (flare-2(A), flare-2(B), flare-2(C), flare-2(D), flare-2(E)) in various periods, which are presented in Figures 4–8, respectively.

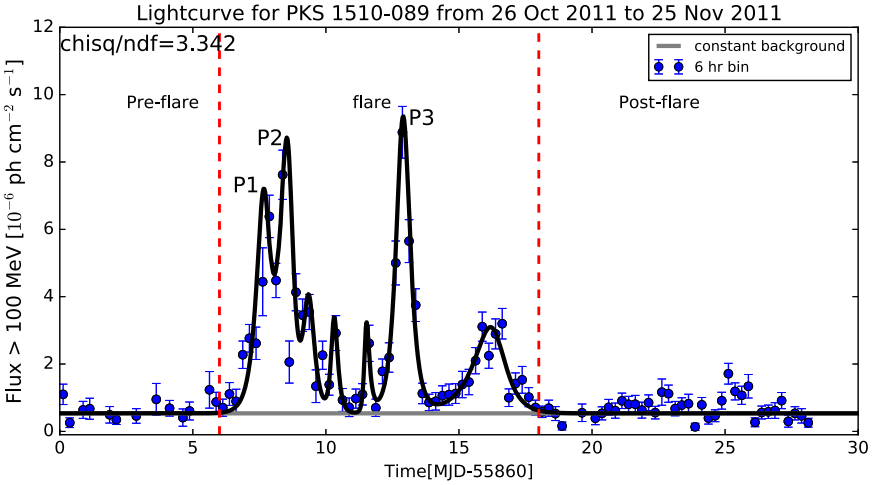

Figure 7. Light curve for flare-2(D) fitted by the sum of exponentials (see the text for details). The fitted parameters are given in Table 2. All of the different periods of activity have been separated by dashed red lines, and the light gray line represents the constant state or flux.

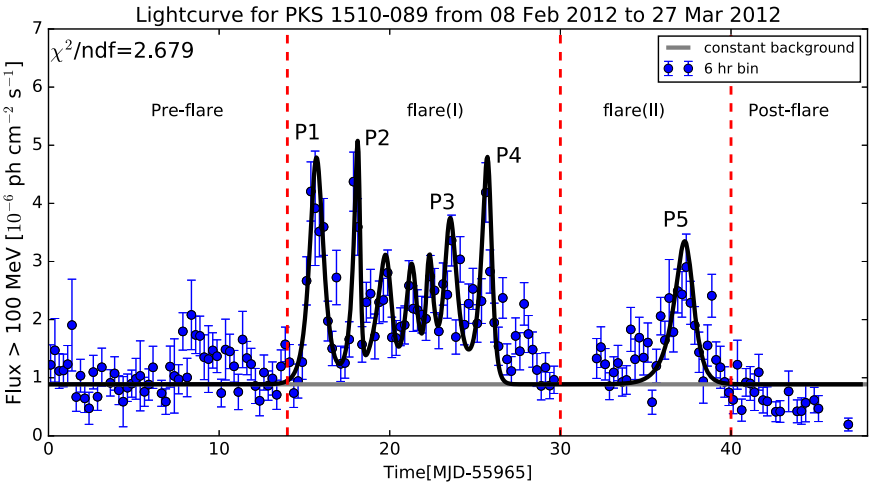

Figure 8. Light curve for flare-2(E) fitted by the sum of exponentials (see the text for details). The fitted parameters are given in Table 2. All of the different periods of activity have been separated by dashed red lines, and the light gray line represents the constant state or flux.

Five activity phases have been observed in flare-2(A). A pre-flare was observed with a flux close to the quiescent state during the time period MJD 55732.0 to 55737.5. During MJD 55737.5–55741.0 (denoted by flare(I) as was done in the case of Flare-1), the flux starts rising from MJD 55737.9 and goes above 2.0, which is denoted as peak P1 ($F_{\rm GeV} = 2.26 \pm 0.52$) at MJD 55738.9. After spending 3 days in the flare(I) phase, the source comes back to its quiescent state. However, this duration of quiescence is quite short-lived, and the flux starts rising slowly again. This rising part is considered as a plateau, which has a time duration of MJD 55741.0 to 55743.5 with an average flux of $F_{\rm GeV} = 0.79 \pm 0.10$. The observation period of flare(II), MJD 55743.5 to 55751.0, shows three distinctive peaks P2, P3, and P4 at MJD 55743.9, 55744.9, and 55746.4 with fluxes of $F_{\rm GeV} = 2.37 \pm 0.55$, 3.67 ± 1.02, and 5.40 ± 0.60, respectively. The modeling parameters have been provided in Table 2.

Flare-2(B) shows the three-phase pattern (pre-flare, flare, and post-flare). A pre-flare phase has been observed with flux close to the quiescent state (and it also shows one outlier) and disconnected from the main flare during the time period MJD 55758 to 55765. A flaring activity happened from MJD 55765 to 55771 during which the flux rose up to ∼4.0, denoted by peak P1 ($F_{\rm GeV} = 3.81 \pm 0.46$) at MJD 55767.4, and after spending around five days in the flaring state it returns to the quiescent state, where the flux is almost similar to that of the pre-flare epoch. The source resides in this quiescent state for a long time, and we consider this state as a post-flare from MJD 55771 to 55777. Details of the parameters in these phases are described in Table 2.

The source exhibits a similar three-phase pattern during flare-2(C) as well with a variation in the flux in the pre-flare region, and the subsequent parameters for modeling this flaring episode are presented in Table 2. Incidentally, one of the brightest flares in the history of PKS 1510-089 (Foschini et al. 2013) was recorded during this period. A major peak P1 ($F_{\rm GeV} = 17.56 \pm 1.15$) was observed at MJD 55853.9 accompanied by a pre-flare and post-flare observed during MJD 55846–55851 and MJD 55855–55860, respectively.

In keeping with the earlier substructures, flare-2(D) exhibits the typical phases of pre-flare, flare, and post-flare. The pre-flare and post-flare were observed during MJD 55860–55866

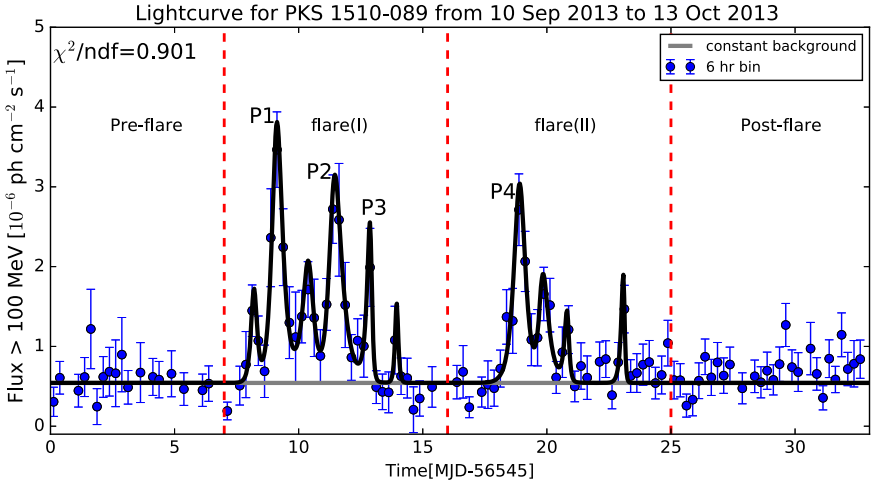

Figure 9. Light curve for flare-3 fitted by the sum of exponentials (see the text for details). The fitted parameters are given in Table 3. All of the different periods of activity have been separated by dashed red lines, and the light gray line represents the constant state or flux.

Table 2
The Same Parameters as Mentioned in Table 1, for Flare-2

Peak	t_0 (MJD)	F_0 (10^{-6} ph cm^{-2} s^{-1})	T_r (hr)	T_d (hr)
		flare-2(A)		
P1	55738.9	2.26 ± 0.52	1.90 ± 1.00	2.67 ± 1.99
P2	55743.9	2.37 ± 0.55	4.70 ± 1.42	3.72 ± 1.44
P3	55744.9	3.67 ± 1.02	4.25 ± 0.93	4.11 ± 0.92
P4	55746.4	5.40 ± 0.60	7.86 ± 0.96	3.98 ± 0.61
		flare-2(B)		
P1	55767.4	3.81 ± 0.46	7.38 ± 0.73	5.10 ± 0.72
		flare-2(C)		
P1	55853.9	17.56 ± 1.15	2.92 ± 0.89	2.50 ± 0.27
		flare-2(D)		
P1	55867.9	6.38 ± 0.63	6.07 ± 1.16	4.74 ± 2.67
P2	55868.4	7.62 ± 0.73	7.08 ± 2.50	3.81 ± 1.43
P3	55872.9	8.88 ± 0.77	5.49 ± 0.75	5.62 ± 0.68
		flare-2(E)		
P1	55980.4	4.20 ± 0.51	8.41 ± 1.36	8.78 ± 1.42
P2	55982.9	4.37 ± 0.51	6.91 ± 1.32	2.02 ± 0.65
P3	55988.7	3.36 ± 0.44	7.06 ± 2.86	9.39 ± 1.96
P3	55990.6	4.19 ± 0.51	8.64 ± 1.42	4.46 ± 1.03
P4	56002.4	2.90 ± 0.57	15.07 ± 2.72	9.50 ± 2.29

and MJD 55878–55890. Three major peaks P1, P2, and P3 were observed during the flaring episode, where the fluxes were $F_{\rm GeV} = 6.38 \pm 0.63$, 7.62 ± 0.73, and 8.88 ± 0.77 at MJD 55867.9, 55868.4, and 55872.9, respectively. Peak P3 claims the distinction of becoming the second-highest peak in the history of PKS 1510-089. The modeling parameters are described in Table 2.

A four-phase pattern (pre-flare, flare(I), flare(II), and post-flare) was observed during MJD 55965–56013, which we refer to as flare-2(E). During the pre-flare part, slight fluctuations are noticed in the flux around the value 1.0. flare(I) is composed of four distinct, major peaks P1, P2, P3, and P4 at MJD 55980.4, 55982.9, 55988.7, and 55990.6 with fluxes of $F_{\rm GeV} = 4.20 \pm 0.51$, 4.37 ± 0.51, 3.36 ± 0.44, and 4.19 ± 0.51, respectively. After spending four to five days in an almost quiescent state, the flux starts rising again from MJD 55998 and shows a clear and major peak P5 at MJD 56002.4 with a flux of $F_{\rm GeV} = 2.90 \pm 0.57$. We refer to this peak as flare(II). During MJD 56005 to 56013, a post-flare was observed whose flux instead of attaining a fixed value keeps fluctuating in the vicinity of the quiescent state flux. The modeling parameters have been described in Table 2.

2.2.3. Flare-3

This is the first time that a detailed study is being done on the flaring episode of PKS 1510-089 during 2013 September 10 to October 13 referred to as Flare-3. The characteristic temporal evolution of the flux of PKS 1510-089 during Flare-3 can be identified by a four-phase pattern (pre-flare, flare(I), flare(II),

Table 3
The Same Parameters as Mentioned in Table 1, for Flare-3

Flare-3				
Peak	t_0 (MJD)	F_0 (10^{-6} ph cm^{-2} s^{-1})	T_r (hr)	T_d (hr)
P1	56554.1	3.47 ± 0.47	3.88 ± 0.89	5.16 ± 0.97
P2	56556.4	2.72 ± 0.43	3.94 ± 0.96	7.02 ± 1.28
P3	56557.9	1.99 ± 0.49	3.12 ± 1.21	1.31 ± 0.94
P4	56563.9	2.71 ± 0.45	4.76 ± 0.92	4.88 ± 0.96

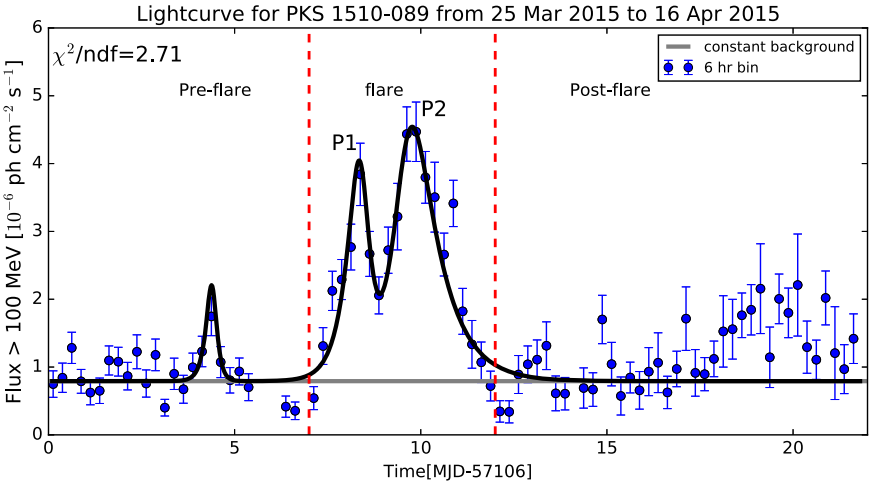

Figure 10. Light curve for flare-4(A) fitted by the sum of exponentials (see the text for details). The fitted parameters are given in Table 4. All of the different periods of activity have been separated by dashed red lines, and the light gray line represents the constant state or flux.

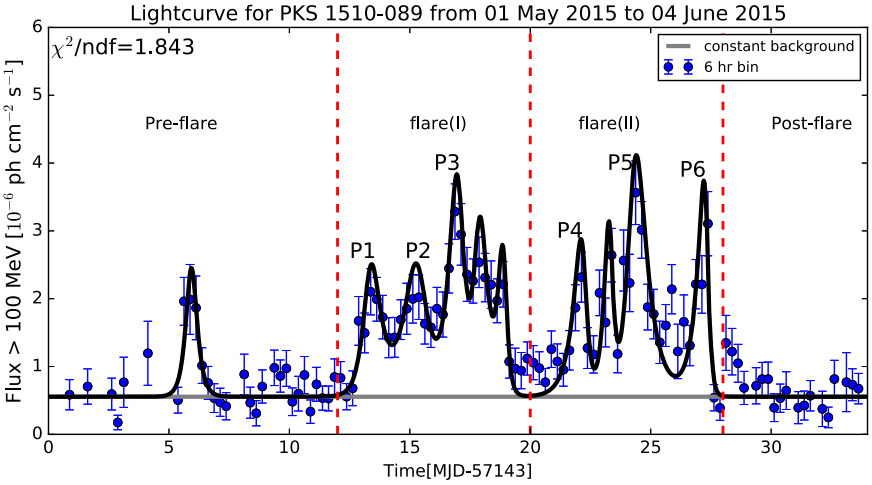

Figure 11. Light curve for flare-4(B) fitted by the sum of exponentials (see the text for details). The fitted parameters are given in Table 4. All of the different periods of activity have been separated by dashed red lines, and the light gray line represents the constant state or flux.

and post-flare). Figure 9 shows a 6 hr bin light curve encompassing all four phases, and the modeling parameters have been provided in Table 3. The pre-flare phase observed during MJD 56545 to 56552 exhibited a fluctuation in the flux around $F_{\rm GeV} = 0.54 \pm 0.02$. flare(I) was observed during MJD 56552–56561, where the flux rises to 3.5. The three peaks P1, P2, and P3 were observed at MJD 56554.1, 56556.4, and 56557.9, and the corresponding fluxes were $F_{\rm GeV} = 3.47 \pm 0.47$, 2.72 ± 0.43, and 1.99 ± 0.49, respectively. After this flaring state, the source spent around two days in its quiescent state, where the flux was around $F_{\rm GeV} = 0.54 \pm 0.02$. The flux again starts rising from MJD 56562.9 and reaches up to $F_{\rm GeV} = 2.71 \pm 0.45$, which is shown by peak P4 at MJD 56563.9. After spending around six days in the second flaring state, the source returns to its quiescent state. A post-flare period started from MJD 56570 and continued until MJD 56578 with the flux remaining steadily below 1.0.

2.2.4. Flare-4

We also carried out a 6 hr binning of Flare-4 (MJD 57082–57265), which revealed the underlying substructures

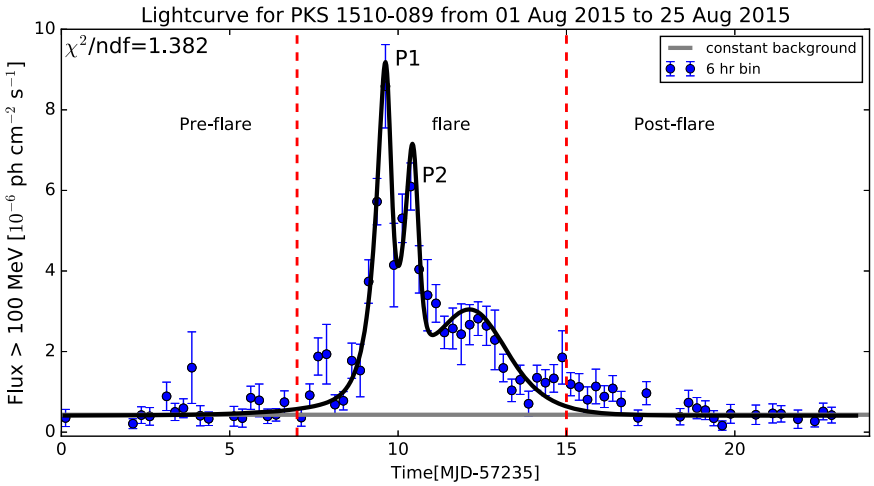

Figure 12. Light curve for flare-4(C) fitted by the sum of exponentials (see the text for details). The fitted parameters are given in Table 4. All of the different periods of activity have been separated by dashed red lines, and the light gray line represents the constant state or flux.

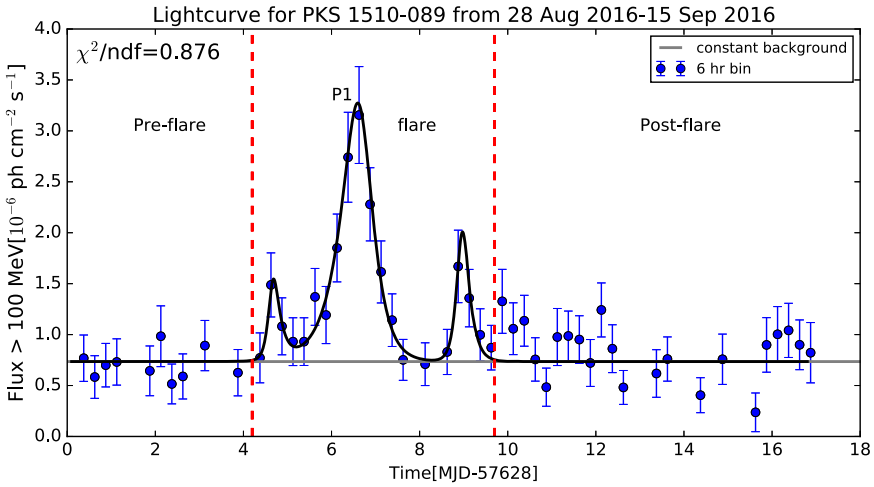

Figure 13. Light curve for flare-5 fitted by the sum of exponentials (see the text for details). The fitted parameters are given in Table 5. All of the different periods of activity have been separated by dashed red lines, and the light gray line represents the constant state or flux.

Table 4
The Same Parameters as Mentioned in Table 1, for Flare-4

Peak	t_0 (MJD)	F_0 (10^{-6} ph cm^{-2} s^{-1})	T_r (hr)	T_d (hr)
		flare-4(A)		
P1	57114.4	3.84 ± 0.46	8.29 ± 1.69	4.93 ± 2.40
P2	57115.9	4.47 ± 0.44	8.27 ± 2.98	18.10 ± 2.27
		flare-4(B)		
P1	57156.4	2.10 ± 0.34	6.83 ± 2.12	9.50 ± 3.99
P2	57158.4	2.02 ± 0.33	11.77 ± 4.48	9.49 ± 3.84
P3	57159.9	3.28 ± 0.41	8.00 ± 2.27	5.35 ± 2.92
P4	57165.1	2.32 ± 0.37	9.87 ± 1.83	3.99 ± 1.56
P5	57167.4	3.56 ± 0.47	6.35 ± 2.09	11.82 ± 1.61
P6	57170.4	3.10 ± 0.47	8.53 ± 1.60	2.67 ± 0.87
		flare-4(C)		
P1	57244.6	8.58 ± 1.03	7.59 ± 0.85	2.66 ± 0.98
P2	57245.4	6.09 ± 0.58	7.11 ± 1.68	2.86 ± 0.80

Table 5
The Same Parameters as Mentioned in Table 1, for Flare-5

Flare-5				
Peak	t_0 (MJD)	F_0 (10^{-6} ph cm^{-2} s^{-1})	T_r (hr)	T_d (hr)
P1	57634.6	3.15 ± 0.47	8.96 ± 1.06	6.28 ± 0.89

Table 6
Values of Constant Flux That Are Also Fitted with the Listed Peaks in the Light Curve

flares/Subflares	Constant flux Flux $F_{0.1-300\ \mathrm{GeV}}$ (10^{-6} ph cm^{-2} s^{-1})
flare-1(A)	0.64 ± 0.07
flare-1(B)	0.61 ± 0.04
flare-2(A)	0.15 ± 0.03
flare-2(B)	0.35 ± 0.03
flare-2(C)	0.74 ± 0.09
flare-2(D)	0.53 ± 0.05
flare-2(E)	0.88 ± 0.04
Flare-3	0.54 ± 0.02
flare-4(A)	0.69 ± 0.05
flare-4(B)	0.50 ± 0.04
flare-4(C)	0.41 ± 0.04
Flare-5	0.74 ± 0.04

Note. A histogram of the constant fluxes in different periods is shown in the left panel of Figure 28.

with the three distinctive features flare-4(A), flare-4(B), and flare-4(C). Figures 10–12 show these substructures along with their different phases.

Flare-4(A) displays the usual three-phase pattern (pre-flare, flare, post-flare). The details of the phase pattern are described in Table 4. The pre-flare and post-flare were observed before and after the flaring state during MJD 57106–57113 and MJD 57118–57128. Even though there are substantial variations in the flux in both the pre-flare and post-flare regions, they are disconnected from the main flare under consideration and are hence not included in the analysis. The flaring duration lasted from MJD 57113 to 57118, during which the flux rose up to a value of 4.5. Two peaks P1 and P2 are clearly seen at MJD 57114.4 and 57115.9 with fluxes of $F_{\mathrm{GeV}} = 3.84 \pm 0.46$ and 4.47 ± 0.44, respectively.

flare-4(B) shows a four phase pattern (pre-flare, flare(I), flare(II), post-flare) with flux variations in the pre-flare region. The detailed study is provided in Table 4. flare(I) was observed during MJD 57155 to 57163, where the flux reached a maximum of $F_{\mathrm{GeV}} = 3.28 \pm 0.41$ (P3). The peaks P1, P2, and P3 at MJD 57156.4, 57158.4, and 57159.9 notch up the peak fluxes of $F_{\mathrm{GeV}} = 2.10 \pm 0.34$, 2.02 ± 0.33, and 3.28 ± 0.41, respectively. After spending around seven days in the flaring state, the source descends to its quiescent state where the flux is comparable to the pre-flare value. The source remains in this state for a duration of 2.5 days. Surprisingly, the flux again starts rising from MJD 57163 and reaches a maximum flux of $F_{\mathrm{GeV}} = 3.56 \pm 0.47$ (P5). This flare, referred to as flare(II), was observed from MJD 57163 to 57171, during which three major peaks P4, P5, and P6 were noticed at MJD 57165.1, 57167.4, and 57170.4. The corresponding fluxes for these peaks were found to be $F_{\mathrm{GeV}} = 2.32 \pm 0.37$, 3.56 ± 0.47, and 3.10 ± 0.47, respectively. The post-flare epoch lasted from MJD 57171 to 57177 with a flux of around 1.0.

flare-4(C) was recorded as the third-brightest flare in the history of PKS 1510-089. The flaring episode lasted from MJD 57242 to 57250, during which the flux rose up to ∼8.60. Two major peaks P1 and P2 were observed at MJD 57244.6 and 57245.4 with a flux of $F_{\mathrm{GeV}} = 8.58 \pm 1.03$ and 6.09 ± 0.58, respectively. A pre-flare (MJD 57235 to 57242) and post-flare (MJD 57250 to 57259) were also observed with similar characteristics. For both the pre-flare and post-flare states, the flux remains below 1.0. The details about the parameters have been provided in Table 4.

2.2.5. Flare-5

Another flare was observed in 2016 August to September during MJD 57628–57646. The maximum flux reached $F_{\mathrm{GeV}} = 3.15 \pm 0.47$ with TS = 236.23. A three-phase pattern (pre-flare, flare, post-flare) was observed during MJD 57628–57646. A clear peak P1 was observed in the flare phase at MJD 57634.625 (Figure 13). Peak P1 was fitted with the function given in Equation (4), and the rising and decay times have been provided in Table 5.

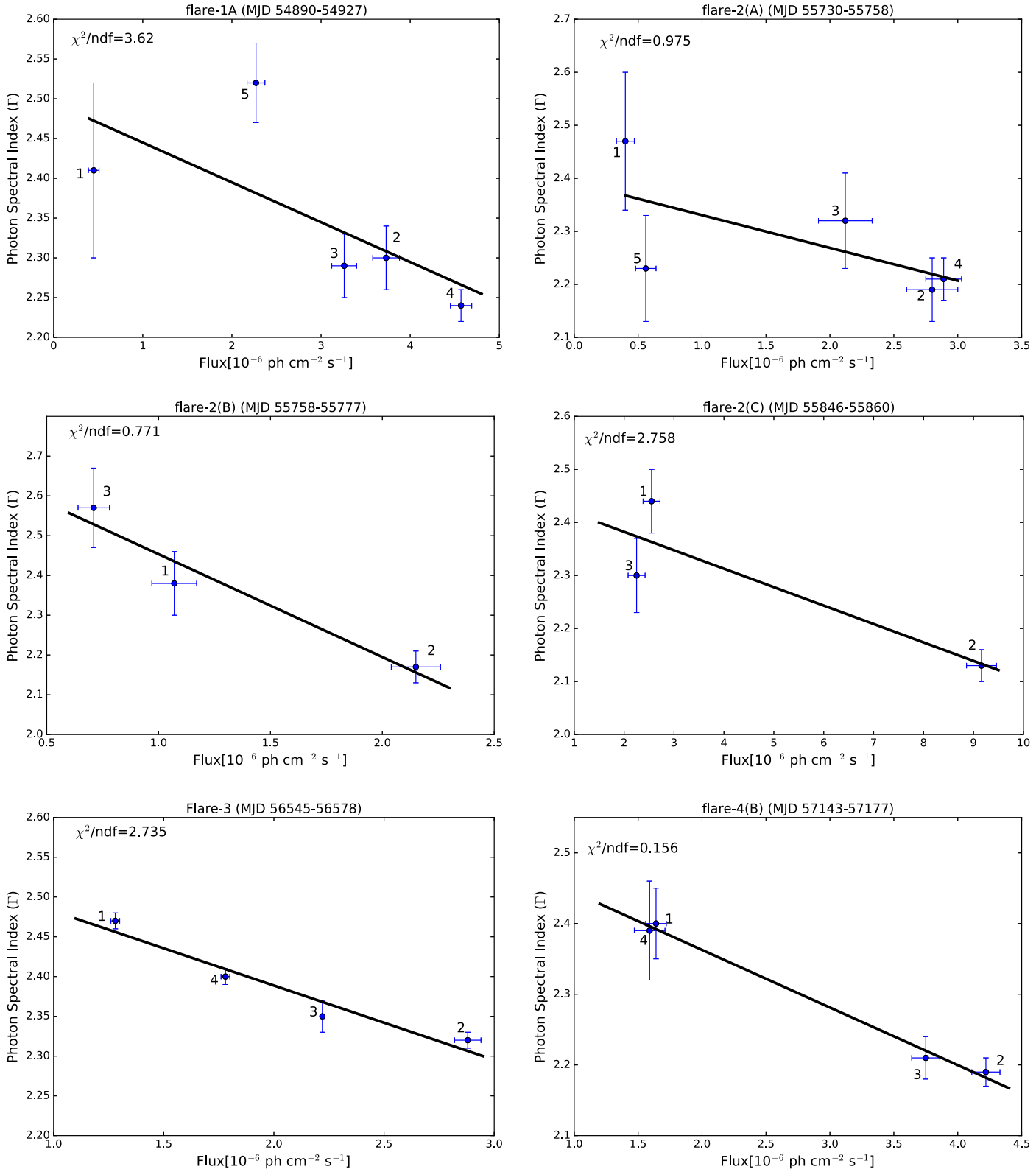

Figure 14. Photon index vs. flux plotted for a few subflares. The numbers 1–5 represent the different time periods. Top panel: 1–5 represent the pre-flare, flare(I), plateau, flare(II), and post-flare states, respectively. Middle panel: 1–3 represent the pre-flare, flare, and post-flare, respectively. Bottom panel: 1–4 represent the pre-flare, flare(I), flare(II), and post-flare, respectively. All of the points have been fitted by the PL spectral type, and the corresponding reduced χ^2 values are mentioned in the plots. Errors associated with each data point are statistical only.

All of the above peaks during the flaring episodes were fitted with the constant state (value), the details of which are provided in Table 6.

The photon spectral index as a function of integral flux are plotted in Figure 14 for a few subflares, and the plot is discussed in detailed in the results and discussion section.

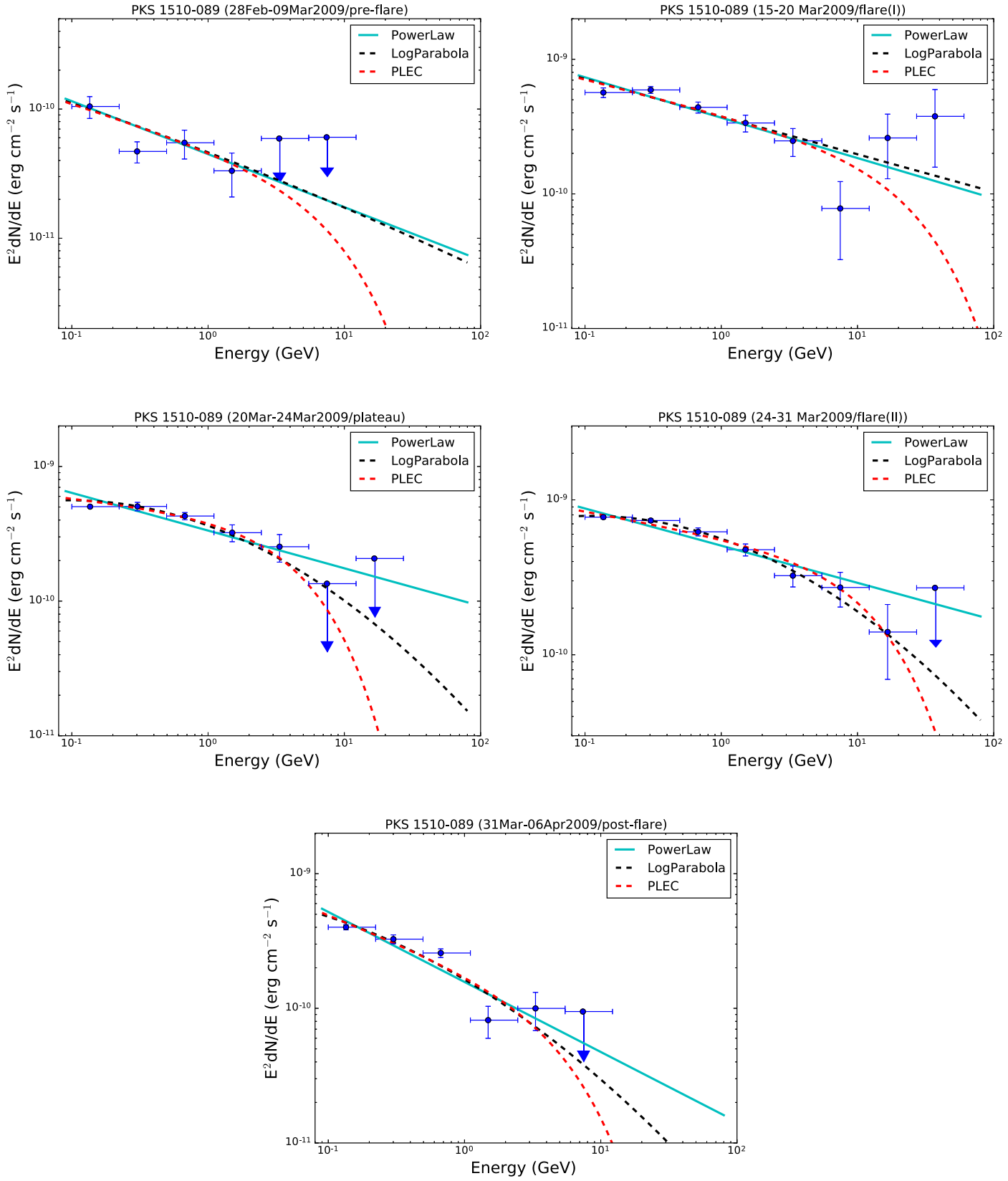

Figure 15. *Fermi*-LAT SEDs during different activity states of flare-1(A) as defined in Figure 2. The PL, LP, and PLEC models are shown in cyan, black, and red, and their respective parameters are given in Table 7.

2.3. SEDs of Flares

This section is dedicated to studying the SEDs of flares and also to report the spectral features that will help us to recognize different phases of the flares. We have produced the SEDs of PKS 1510-089 during different phases of the flares by using three different models, PL, LP, and PLEC, and their functional forms

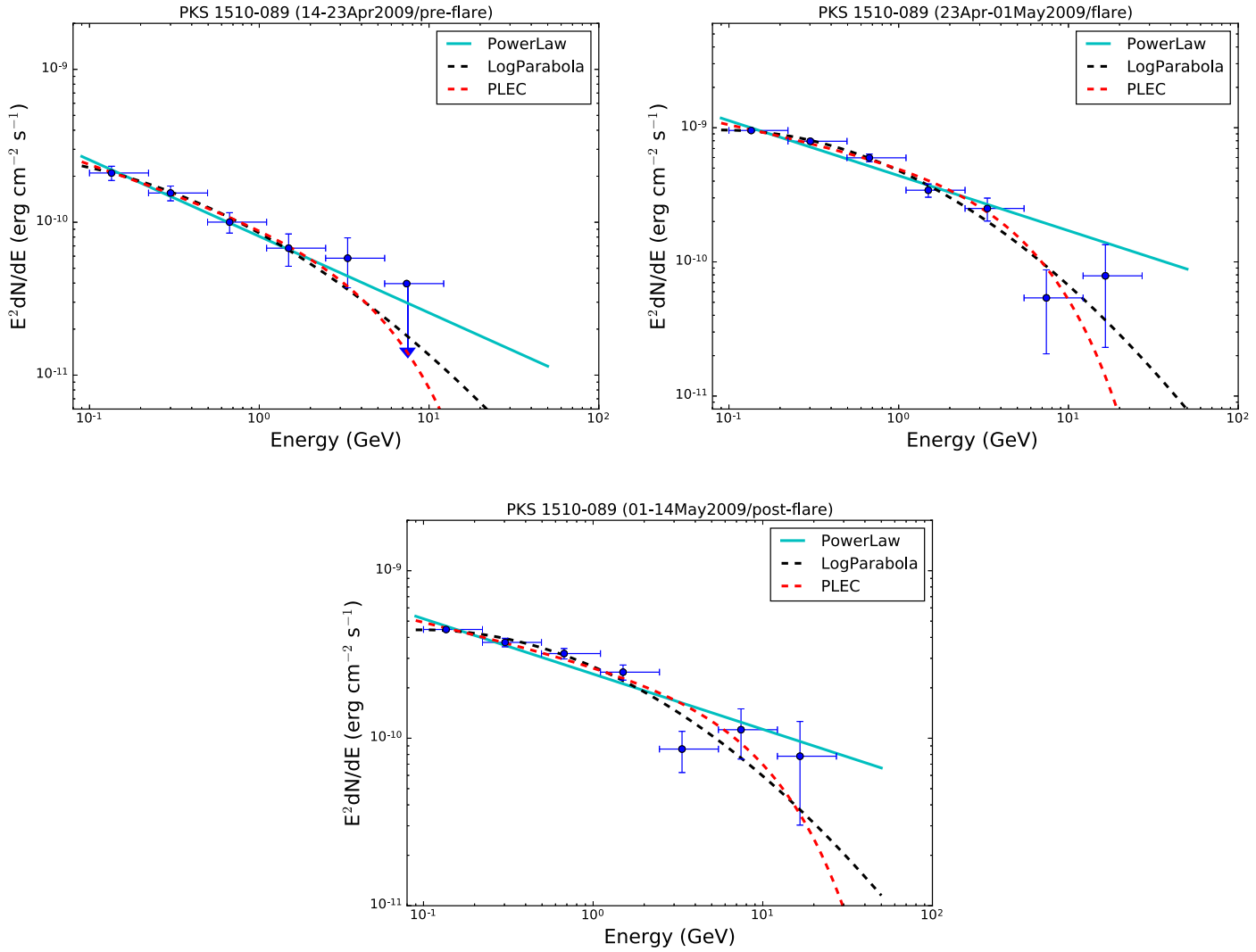

Figure 16. *Fermi*-LAT SEDs during different activity states of flare-1(B) as defined in Figure 3. The PL, LP, and PLEC models are shown in cyan, black and red, and their respective parameters are given in Table 8.

are given in Equations (1)–(3), respectively. We note that in all spectral models the choice of reference energy does not affect the spectral shape (Abdo et al. 2010a). It is fixed at 100 MeV for PL, at 300 MeV for LP, and at 200 Mev for PLEC.

The spectral models (PL, LP, and PLEC) have been plotted with the spectral data points in cyan, black, and red, respectively. Figures 15 and 16 show the spectral analysis of flare-1(A) and flare-1(B), and their corresponding fitted parameters are given in Tables 7 and 8. The log(likelihood) and Δlog(likelihood) were calculated for each and every phase pattern, where Δlog (likelihood) is defined as $\Delta \log(\mathcal{L}) = (\log \mathcal{L}$ (log-parabola/PLEC)–log $\mathcal{L}$(PL)), where $\mathcal{L}$ = likelihood. A progressive spectral hardening is noticed in flare-1(A) and flare-1(B) with increasing flux from one phase to another.

Hardening in the spectrum is noticed during flare-2(A), 2(B), 2(C), 2(D), and 2(E) as the flux increases from the pre-flare to the flare phase. Flare-2(B), 2(C), and 2(D) have shown significant spectral hardening as we move from pre-flare to flare, with the value of the spectral index Γ changing from 2.38 ± 0.08 to 2.17 ± 0.04, 2.44 ± 0.06 to 2.13 ± 0.03, and 2.65 ± 0.10 to 2.24 ± 0.02 when fitted with the PL distribution.

The SEDs for all of the subflares of Flare-2 are plotted in Figures 17–21, and the parameters describing all of these subflares are provided in Tables 9–13.

Flare-3 shows progressive spectral hardening with increasing flux: $\Gamma = 2.47 \pm 0.01$ changes to 2.35 ± 0.00 and 2.32 ± 0.01 (PL fit), which are plotted in Figure 22. The values of the fitted parameters are displayed in Table 14.

A significant amount of spectral hardening is also seen in the subflares of Flare-4. For flare-4(A) and 4(B), the progressive spectral hardening with increasing flux is seen as Γ decreases from 2.32 ± 0.03 to 2.14 ± 0.02 and 2.40 ± 0.05 to 2.19 ± 0.02 in the PL fit. flare-4(C) also shows significant spectral hardening with increasing flux from pre-flare to flare as Γ decreases from 2.42 ± 0.09 to 1.96 ± 0.02 in the PL fit. Their SEDs are shown in Figures 23–25, and the values of the fitted parameters are provided in Tables 15–17, respectively.

A progressive spectral hardening with increasing flux during pre-flare ($\Gamma = 2.58 \pm 0.08$) to flare ($\Gamma = 2.39 \pm 0.04$) is also

Table 7
Results of SEDs Fitted with Different Spectral Types PL, LP, and PLEC

Power Law (PL)					
Activity	$F_{0.1-300\ \mathrm{GeV}}$ (10^{-6} ph cm^{-2} s^{-1})	Γ		−log(Likelihood)	
pre-flare	0.45 ± 0.06	2.41 ± 0.11	⋯	24496.5	⋯
flare(I)	3.73 ± 0.15	2.30 ± 0.04	⋯	20608.5	⋯
plateau	3.26 ± 0.14	2.29 ± 0.04	⋯	20170.3	⋯
flare(II)	4.57 ± 0.12	2.24 ± 0.02	⋯	38286.7	⋯
post-flare	2.27 ± 0.10	2.52 ± 0.05	⋯	24715.6	⋯
Log Parabola (LP)					
Activity	$F_{0.1-300\ \mathrm{GeV}}$ (10^{-6} ph cm^{-2} s^{-1})	α	β	−log(Likelihood)	Δlog(Likelihood)
pre-flare	0.44 ± 0.06	2.40 ± 0.15	0.00 ± 0.00	24496.5	0.0
flare(I)	3.72 ± 0.15	2.28 ± 0.05	0.00 ± 0.00	20608.5	0.0
plateau	3.18 ± 0.14	2.18 ± 0.06	0.08 ± 0.03	20166.4	−3.9
flare(II)	4.45 ± 0.12	2.14 ± 0.04	0.07 ± 0.02	38279.2	−7.5
post-flare	2.24 ± 0.10	2.46 ± 0.06	0.06 ± 0.04	24714.2	−1.4
PLExpCutoff (PLEC)					
Activity	$F_{0.1-300\ \mathrm{GeV}}$ (10^{-6} ph cm^{-2} s^{-1})	Γ_{PLEC}	E_{cutoff} (GeV)	−log(Likelihood)	Δlog(Likelihood)
pre-flare	0.44 ± 0.06	2.32 ± 0.15	9.359 ± 7.506	24496.3	−0.2
flare(I)	3.71 ± 0.15	2.26 ± 0.04	30.000 ± 0.253	20610.0	1.5
plateau	3.18 ± 0.14	2.11 ± 0.08	5.185 ± 2.394	20164.8	−5.5
flare(II)	4.50 ± 0.12	2.16 ± 0.04	15.980 ± 6.358	38281.0	−5.7
post-flare	2.24 ± 0.10	2.40 ± 0.08	6.081 ± 3.856	24713.4	−2.2

Note. Different periods of activity of the flares (here flare-1(A)) are mentioned in the first column. The fitted fluxes and the spectral indices are shown in columns 2 and 3. The goodness of unbinned fits by log(likelihood) is given in column 5, and the Δlog(likelihood) is calculated with respect to the log(likelihood) of the PL fit (see the text for more details).

Table 8
The Same Parameters as Mentioned in Table 7, for flare-1(B)

Power Law (PL)					
Activity	$F_{0.1-300\ \mathrm{GeV}}$ (10^{-6} ph cm^{-2} s^{-1})	Γ		−log(Likelihood)	
pre-flare	1.12 ± 0.07	2.50 ± 0.06	⋯	33110.1	⋯
flare	5.20 ± 0.15	2.41 ± 0.03	⋯	36271.2	⋯
post-flare	2.56 ± 0.09	2.33 ± 0.03	⋯	49194.4	⋯
Log Parabola (LP)					
Activity	$F_{0.1-300\ \mathrm{GeV}}$ (10^{-6} ph cm^{-2} s^{-1})	α	β	−log(Likelihood)	Δlog(Likelihood)
pre-flare	1.10 ± 0.07	2.42 ± 0.08	0.08 ± 0.05	33108.8	−1.3
flare	5.05 ± 0.15	2.30 ± 0.04	0.11 ± 0.03	36260.6	−10.6
post-flare	2.48 ± 0.09	2.21 ± 0.05	0.09 ± 0.03	49187.9	−6.5
PLExpCutoff (PLEC)					
Activity	$F_{0.1-300\ \mathrm{GeV}}$ (10^{-6} ph cm^{-2} s^{-1})	Γ_{PLEC}	E_{cutoff} (GeV)	−log(Likelihood)	Δlog(Likelihood)
pre-flare	1.10 ± 0.07	2.37 ± 0.10	5.948 ± 4.510	33108.5	−1.6
flare	5.10 ± 0.15	2.27 ± 0.05	5.740 ± 1.830	36262.9	−8.3
post-flare	2.52 ± 0.09	2.24 ± 0.05	11.670 ± 5.692	49191.0	−3.4

noted in Flare-5. The SED is shown in Figure 26, and the values of the fitted parameters are provided in Table 18.

In Figure 14 we have plotted the photon spectral index as a function of integrated flux (F_0) for a few subflares. Our plots clearly show spectral hardening with increasing flux. The spectral hardening with increasing flux has been seen previously in many other sources, like 3C 454.3 (Britto et al. 2016) and Mrk 501 (Albert et al. 2007).

Table 9
The Same Parameters as Mentioned in Table 7, for flare-2(A)

Power Law (PL)					
Activity	$F_{0.1-300\ \mathrm{GeV}}$ (10^{-6} ph cm^{-2} s^{-1})	Γ		−log(Likelihood)	
pre-flare	0.40 ± 0.07	2.22 ± 0.13	⋯	14835.3	⋯
flare(I)	2.80 ± 0.20	2.19 ± 0.06	⋯	9462.8	⋯
plateau	2.12 ± 0.21	2.32 ± 0.09	⋯	6705.2	⋯
flare(II)	2.89 ± 0.14	2.21 ± 0.04	⋯	21374.7	⋯
post-flare	0.56 ± 0.08	2.23 ± 0.10	⋯	15417.3	⋯
Log Parabola (LP)					
Activity	$F_{0.1-300\ \mathrm{GeV}}$ (10^{-6} ph cm^{-2} s^{-1})	α	β	log(Likelihood)	Δlog(Likelihood)
pre-flare	0.39 ± 0.07	2.13 ± 0.21	0.04 ± 0.08	14835.1	−0.2
flare(I)	2.68 ± 0.21	2.06 ± 0.10	0.07 ± 0.05	9461.2	−1.6
plateau	1.79 ± 0.21	2.07 ± 0.15	0.10 ± 0.07	6697.8	−7.4
flare(II)	2.65 ± 0.14	1.95 ± 0.07	0.17 ± 0.04	21362.3	−12.4
post-flare	0.50 ± 0.08	1.97 ± 0.21	0.14 ± 0.10	15416.0	−1.3
PLExpCutoff (PLEC)					
Activity	$F_{0.1-300\ \mathrm{GeV}}$ (10^{-6} ph cm^{-2} s^{-1})	Γ_{PLEC}	E_{cutoff} (GeV)	−log(Likelihood)	Δlog(Likelihood)
pre-flare	0.38 ± 0.07	2.08 ± 0.22	9.546 ± 12.560	14834.6	−0.7
flare(I)	2.71 ± 0.20	2.07 ± 0.10	11.270 ± 8.127	9461.0	−1.8
plateau	1.80 ± 0.21	2.03 ± 0.16	5.316 ± 4.204	6697.3	−7.9
flare(II)	2.69 ± 0.14	1.86 ± 0.09	2.699 ± 0.733	21359.9	−14.8
post-flare	0.51 ± 0.08	1.94 ± 0.21	4.121 ± 3.184	15415.7	−1.6

Table 10
The Same Parameters as Mentioned in Table 7, for flare-2(B)

Power Law (PL)					
Activity	$F_{0.1-300\ \mathrm{GeV}}$ (10^{-6} ph cm^{-2} s^{-1})	Γ		−log(Likelihood)	
pre-flare	1.07 ± 0.10	2.38 ± 0.08	⋯	17894.3	⋯
flare	2.15 ± 0.11	2.17 ± 0.04	⋯	21202.8	⋯
post-flare	0.71 ± 0.07	2.57 ± 0.10	⋯	20681.9	⋯
Log Parabola (LP)					
Activity	$F_{0.1-300\ \mathrm{GeV}}$ (10^{-6} ph cm^{-2} s^{-1})	α	β	−log(Likelihood)	Δlog(Likelihood)
pre-flare	1.02 ± 0.11	2.26 ± 0.13	0.09 ± 0.07	17893.1	−1.2
flare	2.03 ± 0.11	1.97 ± 0.07	0.13 ± 0.04	21196.0	−6.8
post-flare	0.70 ± 0.07	2.48 ± 0.13	0.11 ± 0.10	20681.2	−0.7
PLExpCutoff (PLEC)					
Activity	$F_{0.1-300\ \mathrm{GeV}}$ (10^{-6} ph cm^{-2} s^{-1})	Γ_{PLEC}	E_{cutoff} (GeV)	−log(Likelihood)	Δlog(Likelihood)
pre-flare	1.03 ± 0.10	2.23 ± 0.15	6.094 ± 5.426	17893.1	−1.2
flare	2.06 ± 0.11	1.98 ± 0.08	5.818 ± 2.364	21196.6	−6.2
post-flare	0.70 ± 0.07	2.46 ± 0.17	6.339 ± 8.688	20681.5	−0.4

Table 11
The Same Parameters as Mentioned in Table 7, for flare-2(C)

Power Law (PL)					
Activity	$F_{0.1-300\ \mathrm{GeV}}$ (10^{-6} ph cm^{-2} s^{-1})	Γ		−log(Likelihood)	
pre-flare	2.55 ± 0.17	2.44 ± 0.06	⋯	13635.9	⋯
flare	9.16 ± 0.30	2.13 ± 0.03	⋯	17028.5	⋯
post-flare	2.25 ± 0.17	2.30 ± 0.07	⋯	11397.9	⋯
Log Parabola (LP)					
Activity	$F_{0.1-300\ \mathrm{GeV}}$ (10^{-6} ph cm^{-2} s^{-1})	α	β	−log(Likelihood)	Δlog(Likelihood)
pre-flare	2.70 ± 0.17	2.45 ± 0.08	0.051 ± 0.050	13642.8	6.9
flare	8.92 ± 0.30	2.03 ± 0.04	0.06 ± 0.02	17023.4	−5.1
post-flare	2.25 ± 0.17	2.30 ± 0.07	0.00 ± 0.00	11397.9	0.0
PLExpCutoff (PLEC)					
Activity	$F_{0.1-300\ \mathrm{GeV}}$ (10^{-6} ph cm^{-2} s^{-1})	Γ_{PLEC}	E_{cutoff} (GeV)	−log(Likelihood)	Δlog(Likelihood)
pre-flare	2.50 ± 0.17	2.34 ± 0.10	9.067 ± 8.024	13634.8	−1.1
flare	9.00 ± 0.31	2.05 ± 0.04	18.030 ± 7.530	17023.2	−5.3
post-flare	2.22 ± 0.17	2.26 ± 0.07	30.000 ± 0.080	11398.6	0.7

Table 12
The Same Parameters as Mentioned in Table 7, for flare-2(D)

Power Law (PL)					
Activity	$F_{0.1-300\ \mathrm{GeV}}$ (10^{-6} ph cm^{-2} s^{-1})	Γ		−log(Likelihood)	
pre-flare	1.45 ± 0.12	2.65 ± 0.10	⋯	14564.0	⋯
flare	5.55 ± 0.13	2.24 ± 0.02	⋯	59688.8	⋯
post-flare	1.65 ± 0.07	2.48 ± 0.04	⋯	47148.3	⋯
Log Parabola (LP)					
Activity	$F_{0.1-300\ \mathrm{GeV}}$ (10^{-6} ph cm^{-2} s^{-1})	α	β	−log(Likelihood)	Δlog(Likelihood)
pre-flare	1.41 ± 0.13	2.55 ± 0.12	0.14 ± 0.10	14562.7	−1.3
flare	5.35 ± 0.13	2.11 ± 0.03	0.09 ± 0.02	59672.5	−16.3
post-flare	1.63 ± 0.07	2.42 ± 0.05	0.05 ± 0.03	47147.0	−1.3
PLExpCutoff (PLEC)					
Activity	$F_{0.1-300\ \mathrm{GeV}}$ (10^{-6} ph cm^{-2} s^{-1})	Γ_{PLEC}	E_{cutoff} (GeV)	−log(Likelihood)	Δlog(Likelihood)
pre-flare	1.42 ± 0.13	2.44 ± 0.18	3.140 ± 2.743	14562.9	−1.9
flare	5.44 ± 0.13	2.14 ± 0.03	12.310 ± 3.515	59677.4	−11.4
post-flare	1.63 ± 0.07	2.38 ± 0.07	8.401 ± 5.696	47146.2	−2.1

Table 13
The Same Parameters as Mentioned in Table 7, for flare-2(E)

Power Law (PL)					
Activity	$F_{0.1-300\ \mathrm{GeV}}$ (10^{-6} ph cm^{-2} s^{-1})	Γ		−log(Likelihood)	
pre-flare	2.91 ± 0.09	2.40 ± 0.03	⋯	49012.7	⋯
flare(I)	4.94 ± 0.09	2.29 ± 0.02	⋯	70122.5	⋯
flare(II)	4.13 ± 0.13	2.49 ± 0.03	⋯	26676.5	⋯
post-flare	1.26 ± 1.05	2.64 ± 0.08	⋯	13838.9	⋯
Log Parabola (LP)					
Activity	$F_{0.1-300\ \mathrm{GeV}}$ (10^{-6} ph cm^{-2} s^{-1})	α	β	−log(Likelihood)	Δlog(Likelihood)
pre-flare	2.87 ± 0.10	2.36 ± 0.04	0.03 ± 0.02	49011.6	−1.1
flare(I)	4.78 ± 0.09	2.17 ± 0.02	0.09 ± 0.01	70096.3	−26.2
flare(II)	4.06 ± 0.14	2.44 ± 0.04	0.06 ± 0.03	26674.2	−2.3
post-flare	1.24 ± 0.11	2.58 ± 0.11	0.07 ± 0.06	13838.4	−0.5
PLExpCutoff (PLEC)					
Activity	$F_{0.1-300\ \mathrm{GeV}}$ (10^{-6} ph cm^{-2} s^{-1})	Γ_{PLEC}	E_{cutoff} (GeV)	−log(Likelihood)	Δlog(Likelihood)
pre-flare	2.89 ± 0.09	2.37 ± 0.03	29.970 ± 3.615	49011.7	−1.0
flare(I)	4.83 ± 0.09	2.16 ± 0.03	7.612 ± 1.533	70099.0	−23.5
flare(II)	4.08 ± 0.14	2.41 ± 0.05	9.709 ± 5.118	26673.7	−2.8
post-flare	1.24 ± 0.11	2.54 ± 0.14	7.244 ± 8.785	13838.4	−0.5

Table 14
The Same Parameters as Mentioned in Table 7, for Flare-3

Power Law (PL)					
Activity	$F_{0.1-300\ \mathrm{GeV}}$ (10^{-6} ph cm^{-2} s^{-1})	Γ		−log(Likelihood)	
pre-flare	1.28 ± 0.02	2.47 ± 0.01	⋯	15158.0	⋯
flare(I)	2.88 ± 0.06	2.32 ± 0.01	⋯	24129.8	⋯
flare(II)	2.22 ± 0.01	2.35 ± 0.02	⋯	29884.4	⋯
post-flare	1.78 ± 0.02	2.40 ± 0.01	⋯	30937.3	⋯
Log Parabola (LP)					
Activity	$F_{0.1-300\ \mathrm{GeV}}$ (10^{-6} ph cm^{-2} s^{-1})	α	β	−log(Likelihood)	Δlog(Likelihood)
pre-flare	1.29 ± 0.11	2.45 ± 0.09	0.02 ± 0.00	15158.0	0.0
flare(I)	2.74 ± 0.08	2.19 ± 0.05	0.10 ± 0.04	24123.9	−5.9
flare(II)	2.17 ± 0.06	2.27 ± 0.03	0.06 ± 0.03	29883.2	−1.2
post-flare	1.76 ± 0.08	2.36 ± 0.04	0.04 ± 0.01	30936.7	−0.6
PLExpCutoff (PLEC)					
Activity	$F_{0.1-300\ \mathrm{GeV}}$ (10^{-6} ph cm^{-2} s^{-1})	Γ_{PLEC}	E_{cutoff} (GeV)	log(Likelihood)	Δlog(Likelihood)
pre-flare	1.27 ± 0.10	2.41 ± 0.08	16.580 ± 2.897	15157.1	−0.7
flare(I)	2.78 ± 0.10	2.15 ± 0.05	5.022 ± 0.180	24123.7	−6.1
flare(II)	2.17 ± 0.05	2.24 ± 0.03	9.043 ± 0.223	29881.6	−2.8
post-flare	1.76 ± 0.06	2.35 ± 0.05	18.030 ± 1.724	30936.5	−0.8

Table 15
The Same Parameters as Mentioned in Table 7, for flare-4(A)

Power Law (PL)					
Activity	$F_{0.1-300\ \mathrm{GeV}}$ (10^{-6} ph cm^{-2} s^{-1})	Γ		−log(Likelihood)	
pre-flare	2.21 ± 0.07	2.32 ± 0.03	⋯	50195.9	⋯
flare	6.41 ± 0.17	2.14 ± 0.04	⋯	30084.0	⋯
post-flare	2.92 ± 0.12	2.42 ± 0.04	⋯	34033.0	⋯
Log Parabola (LP)					
Activity	$F_{0.1-300\ \mathrm{GeV}}$ (10^{-6} ph cm^{-2} s^{-1})	α	β	−log(Likelihood)	Δlog(Likelihood)
pre-flare	2.14 ± 0.07	2.20 ± 0.04	0.09 ± 0.03	50188.6	−7.3
flare	6.03 ± 0.18	2.03 ± 0.06	0.06 ± 0.03	30067.9	−16.1
post-flare	2.83 ± 0.12	2.33 ± 0.05	0.08 ± 0.03	34029.4	−3.6
PLExpCutoff (PLEC)					
Activity	$F_{0.1-300\ \mathrm{GeV}}$ (10^{-6} ph cm^{-2} s^{-1})	Γ_{PLEC}	E_{cutoff} (GeV)	−log(Likelihood)	Δlog(Likelihood)
pre-flare	2.17 ± 0.07	2.21 ± 0.05	9.657 ± 3.964	50191.3	−4.6
flare	6.35 ± 0.17	2.04 ± 0.07	12.785 ± 8.115	30080.7	−3.3
post-flare	2.86 ± 0.12	2.32 ± 0.06	9.118 ± 5.157	34030.2	−2.8

Table 16
The Same Parameters as Mentioned in Table 7, for flare-4(B)

Power Law (PL)					
Activity	$F_{0.1-300\ \mathrm{GeV}}$ (10^{-6} ph cm^{-2} s^{-1})	Γ		−log(Likelihood)	
pre-flare	1.64 ± 0.08	2.40 ± 0.05	⋯	38092.3	⋯
flare(I)	4.22 ± 0.11	2.19 ± 0.04	⋯	39757.9	⋯
flare(II)	3.75 ± 0.11	2.20 ± 0.04	⋯	36387.9	⋯
post-flare	1.59 ± 0.12	2.39 ± 0.07	⋯	16506.6	⋯
Log Parabola (LP)					
Activity	$F_{0.1-300\ \mathrm{GeV}}$ (10^{-6} ph cm^{-2} s^{-1})	α	β	−log(Likelihood)	Δlog(Likelihood)
pre-flare	1.62 ± 0.08	2.37 ± 0.06	0.02 ± 0.03	38092.0	−0.3
flare(I)	4.12 ± 0.11	2.09 ± 0.05	0.07 ± 0.00	39749.7	−8.2
flare(II)	3.61 ± 0.11	2.06 ± 0.04	0.10 ± 0.02	36375.6	−12.3
post-flare	1.49 ± 0.12	2.21 ± 0.11	0.15 ± 0.07	16503.3	−3.3
PLExpCutoff (PLEC)					
Activity	$F_{0.1-300\ \mathrm{GeV}}$ (10^{-6} ph cm^{-2} s^{-1})	Γ_{PLEC}	E_{cutoff} (GeV)	−log(Likelihood)	Δlog(Likelihood)
pre-flare	1.62 ± 0.08	2.36 ± 0.05	30.000 ± 0.050	38093.6	1.3
flare(I)	4.14 ± 0.11	2.06 ± 0.05	9.073 ± 0.308	39747.0	−10.9
flare(II)	3.67 ± 0.11	2.08 ± 0.04	9.743 ± 3.159	36378.8	−9.1
post-flare	1.51 ± 0.12	2.12 ± 0.14	3.060 ± 1.610	16503.0	−3.6

Table 17
The Same Parameters as Mentioned in Table 7, for flare-4(C)

Power Law (PL)					
Activity	$F_{0.1-300\ \mathrm{GeV}}$ (10^{-6} ph cm^{-2} s^{-1})	Γ		−log(Likelihood)	
pre-flare	1.15 ± 0.11	2.42 ± 0.09	⋯	15800.4	⋯
flare	4.89 ± 0.15	1.96 ± 0.02	⋯	30002.9	⋯
post-flare	1.22 ± 0.08	2.42 ± 0.06	⋯	27063.2	⋯
Log Parabola (LP)					
Activity	$F_{0.1-300\ \mathrm{GeV}}$ (10^{-6} ph cm^{-2} s^{-1})	α	β	−log(Likelihood)	Δlog(Likelihood)
pre-flare	1.35 ± 0.11	2.55 ± 0.09	0.00 ± 0.00	15817.6	17.2
flare	4.64 ± 0.16	1.81 ± 0.04	0.06 ± 0.01	29993.2	−9.7
post-flare	1.16 ± 0.09	2.29 ± 0.10	0.11 ± 0.06	27061.0	−2.2
PLExpCutoff (PLEC)					
Activity	$F_{0.1-300\ \mathrm{GeV}}$ (10^{-6} ph cm^{-2} s^{-1})	Γ_{PLEC}	E_{cutoff} (GeV)	−log(Likelihood)	Δlog(Likelihood)
pre-flare	1.12 ± 0.11	2.31 ± 0.13	8.931 ± 9.809	15799.8	−0.6
flare	4.75 ± 0.16	1.88 ± 0.03	29.710 ± 8.166	29994.5	−8.4
post-flare	1.19 ± 0.09	2.29 ± 0.11	7.354 ± 5.857	27061.7	−1.5

Table 18
The Same Parameters as Mentioned in Table 7, for flare-5

Power Law (PL)					
Activity	$F_{0.1-300\ \mathrm{GeV}}$ (10^{-6} ph cm^{-2} s^{-1})	Γ		−log(Likelihood)	
pre-flare	1.64 ± 0.12	2.58 ± 0.08	⋯	14412.7	⋯
flare	3.01 ± 0.11	2.39 ± 0.04	⋯	28013.0	⋯
post-flare	1.85 ± 0.09	2.38 ± 0.04	⋯	29145.4	⋯
Log Parabola (LP)					
Activity	$F_{0.1-300\ \mathrm{GeV}}$ (10^{-6} ph cm^{-2} s^{-1})	α	β	−log(Likelihood)	Δlog(Likelihood)
pre-flare	1.63 ± 0.12	2.55 ± 0.10	0.04 ± 0.06	14412.5	−0.2
flare	2.93 ± 0.11	2.28 ± 0.05	0.10 ± 0.03	28007.3	−5.7
post-flare	1.82 ± 0.09	2.31 ± 0.06	0.06 ± 0.04	29143.9	−1.5
PLExpCutoff (PLEC)					
Activity	$F_{0.1-300\ \mathrm{GeV}}$ (10^{-6} ph cm^{-2} s^{-1})	Γ_{PLEC}	E_{cutoff} (GeV)	−log(Likelihood)	Δlog(Likelihood)
pre-flare	1.62 ± 0.12	2.44 ± 0.14	4.640 ± 4.235	14411.7	−1.0
flare	2.95 ± 0.11	2.23 ± 0.07	5.016 ± 2.001	28007.2	−5.8
post-flare	1.83 ± 0.09	2.33 ± 0.06	19.040 ± 17.200	29144.5	−0.9

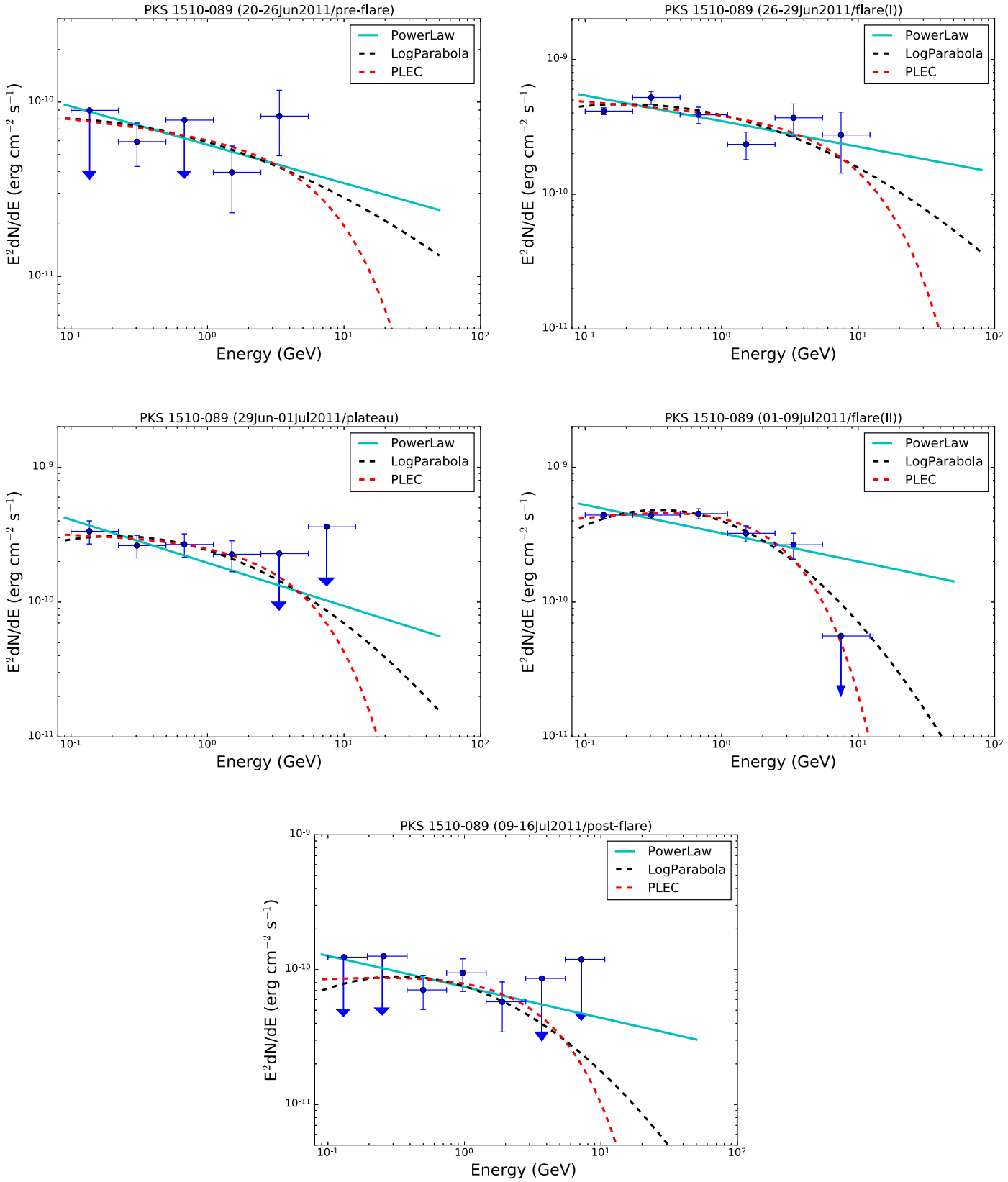

Figure 17. *Fermi*-LAT SEDs during different activity states of flare-2(A) as defined in Figure 4. The PL, LP, and PLEC models are shown in cyan, black and red, and their respective parameters are given in the Table 9.

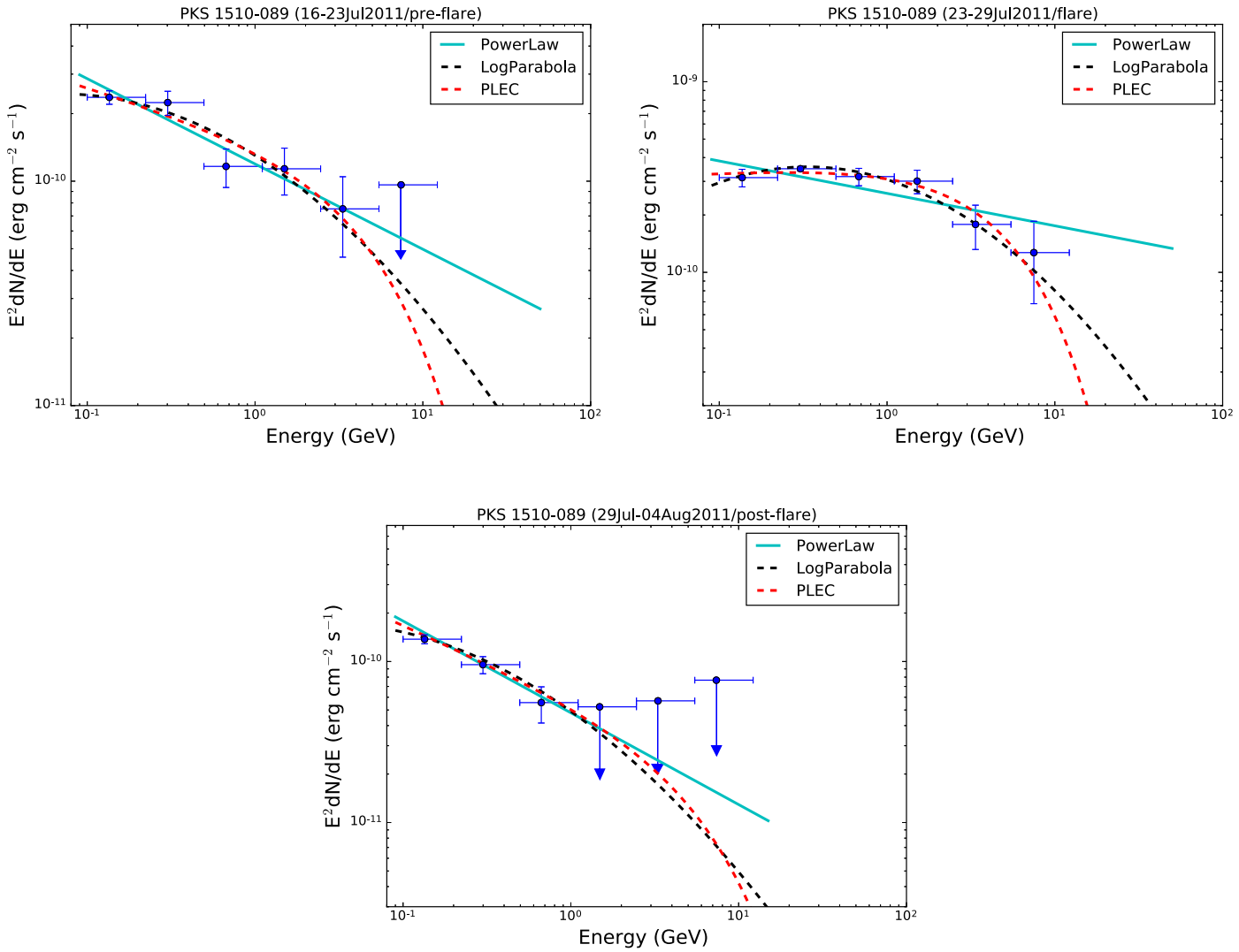

Figure 18. *Fermi*-LAT SEDs during different activity states of flare-2(B) as defined in Figure 5. The PL, LP, and PLEC models are shown in cyan, black and red, and their respective parameters are given in Table 10.

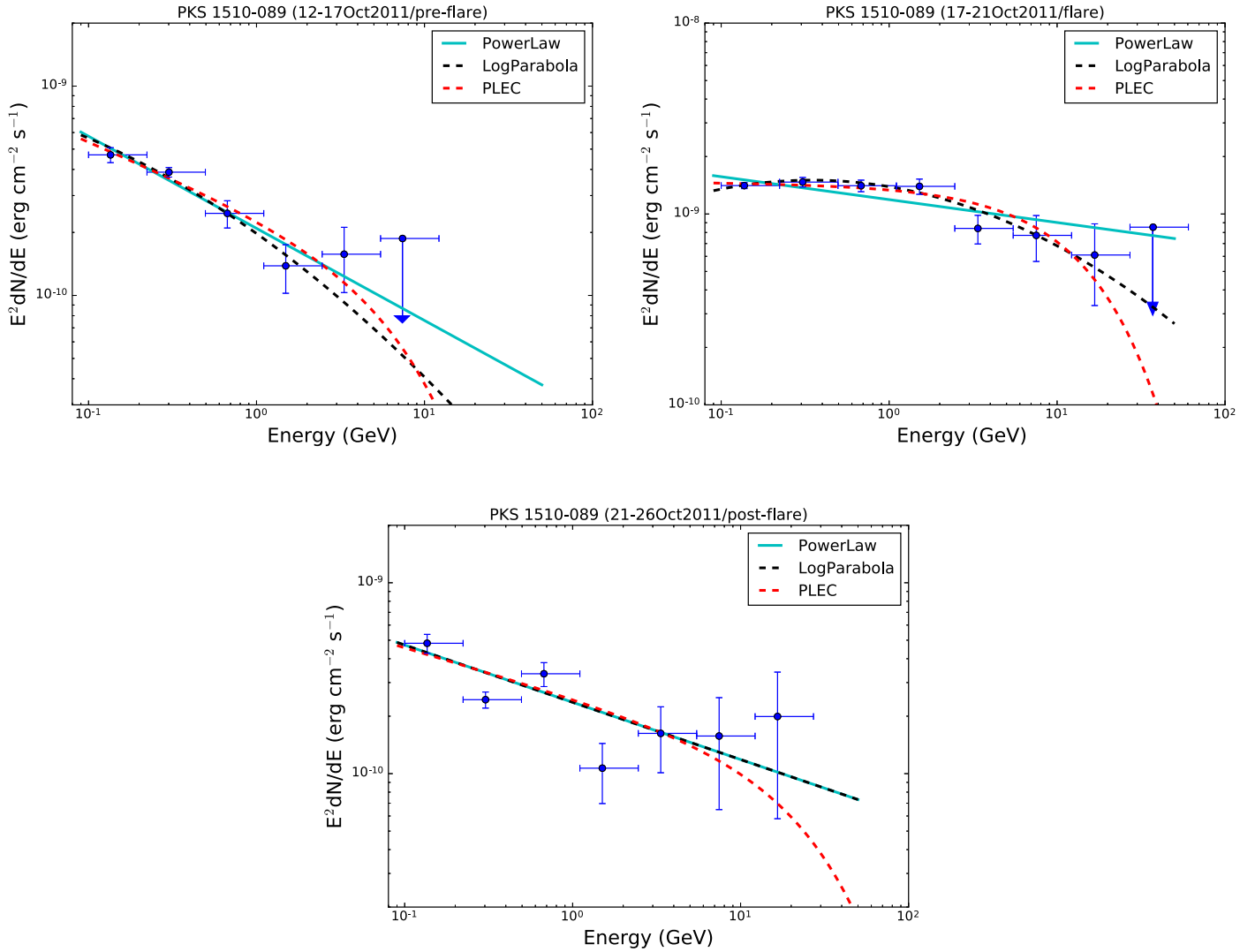

Figure 19. *Fermi*-LAT SEDs during different activity states of flare-2(C) as defined in Figure 6. The PL, LP, and PLEC models are shown in cyan, black and red, and their respective parameters are given in Table 11.

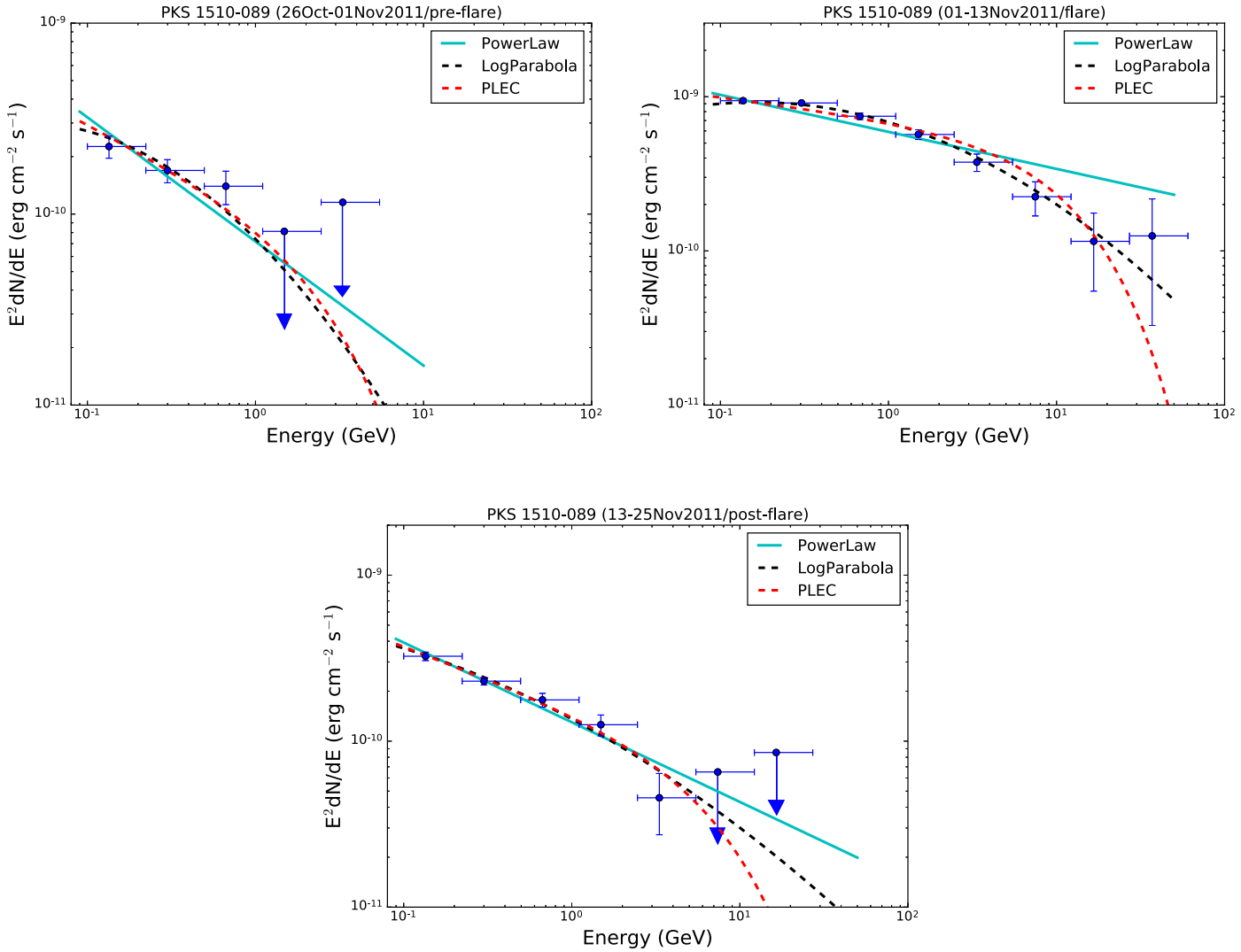

Figure 20. *Fermi*-LAT SEDs during different activity states of flare-2(D) as defined in Figure 7. The PL, LP, and PLEC models are shown in cyan, black and red, and their respective parameters are given in Table 12.

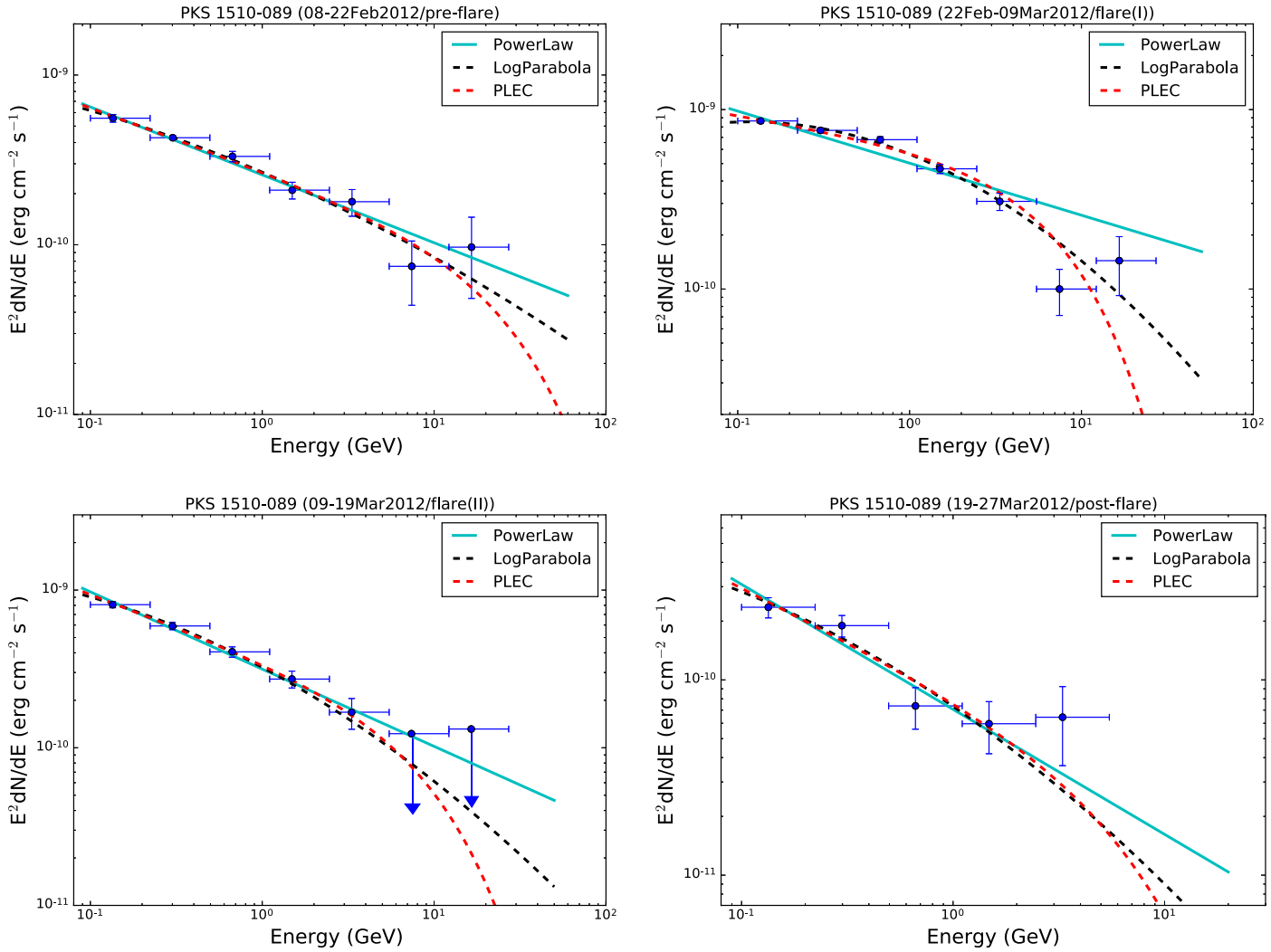

Figure 21. *Fermi*-LAT SEDs during different activity states of flare-2(E) as defined in Figure 8. The PL, LP, and PLEC models are shown in cyan, black and red, and their respective parameters are given in Table 13.

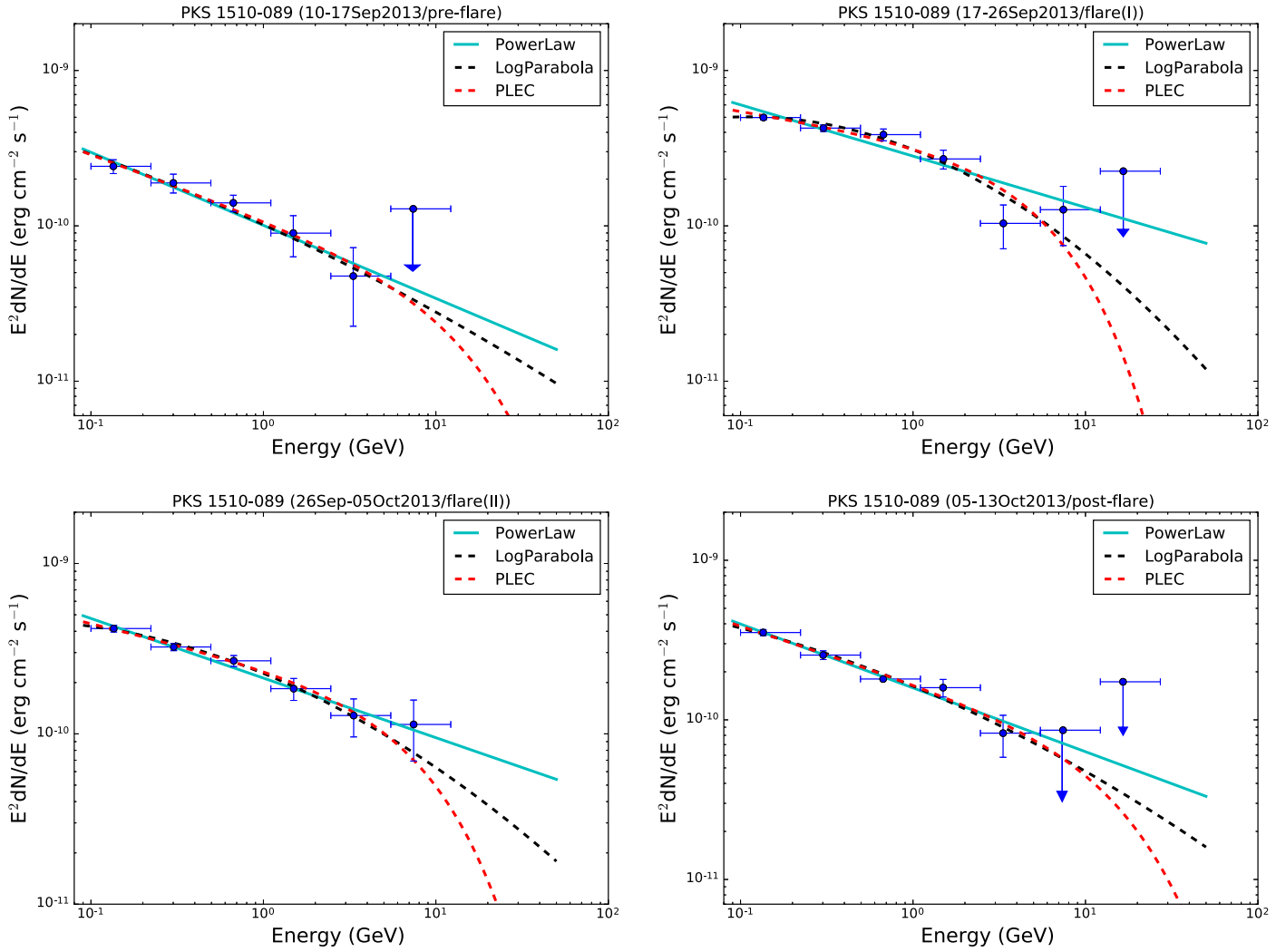

Figure 22. *Fermi*-LAT SEDs during different activity states of flare-3 as defined in Figure 9. The PL, LP, and PLEC models are shown in cyan, black, and red, and their respective parameters are given in Table 14.

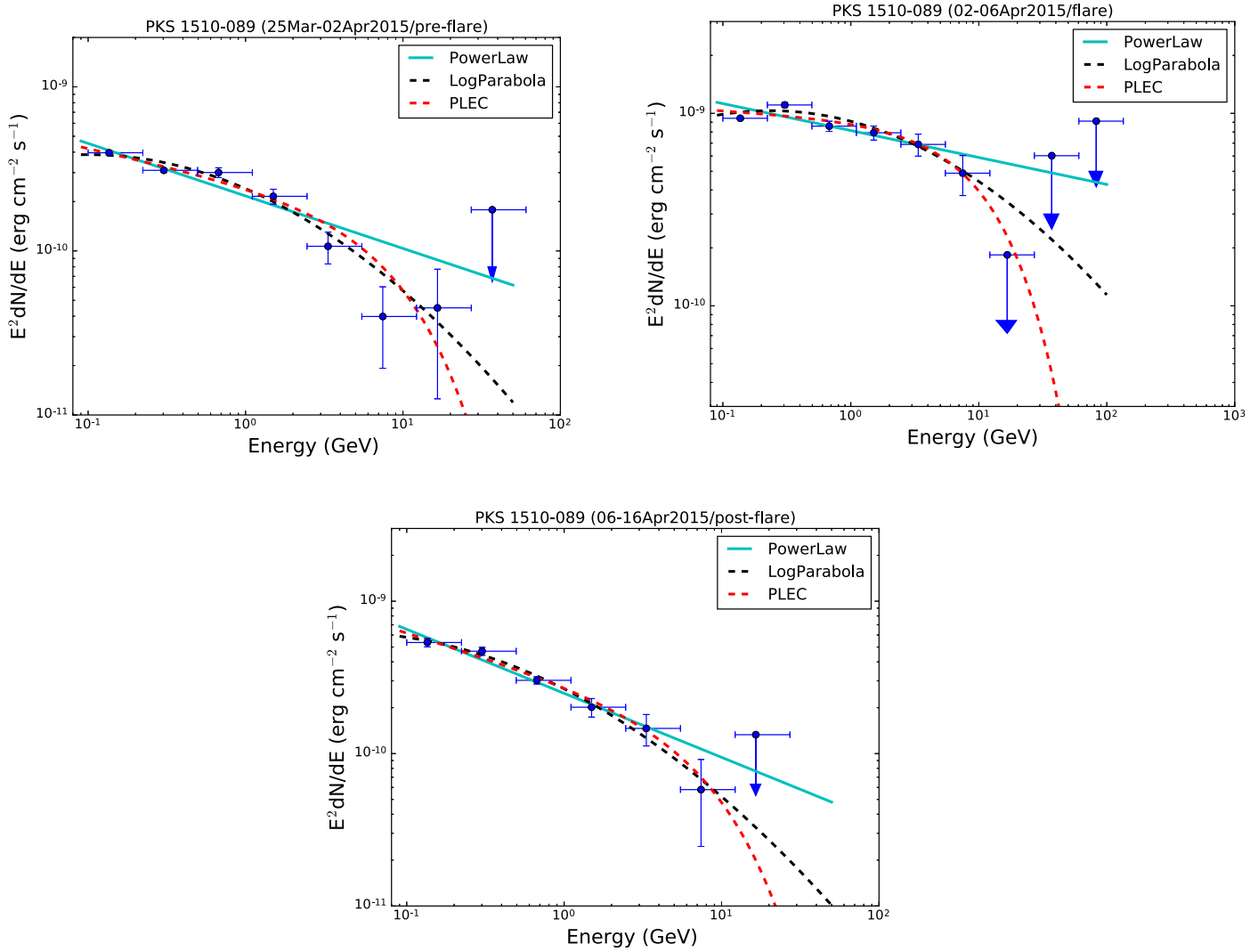

Figure 23. *Fermi*-LAT SEDs during different activity states of flare-4(A) as defined in Figure 10. The PL, LP, and PLEC models are shown in cyan, black, and red, and their respective parameters are given in Table 15.

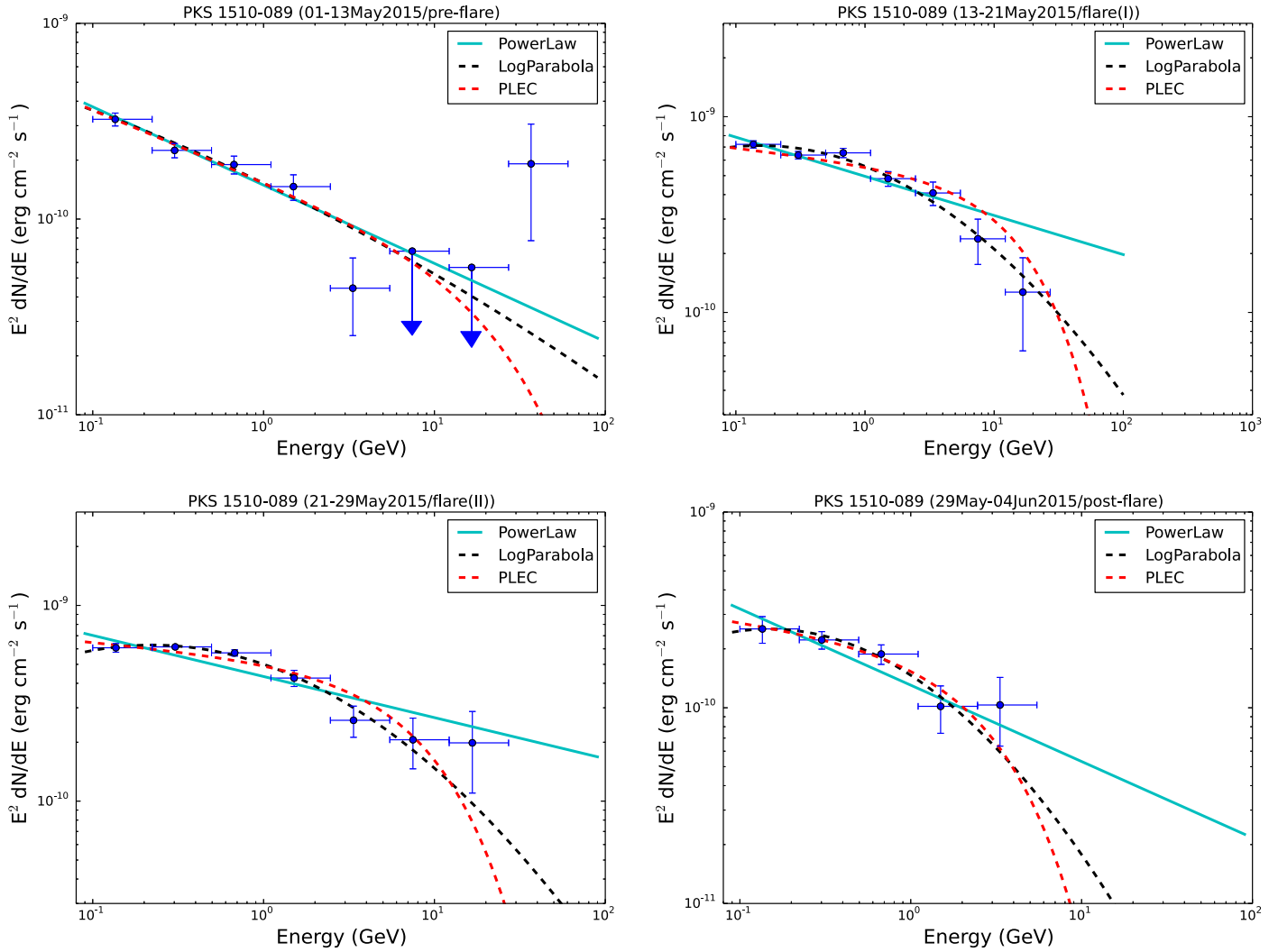

Figure 24. *Fermi*-LAT SEDs during different activity states of flare-4(B) as defined in Figure 11. The PL, LP, and PLEC models are shown in cyan, black, and red, and their respective parameters are given in Table 16.

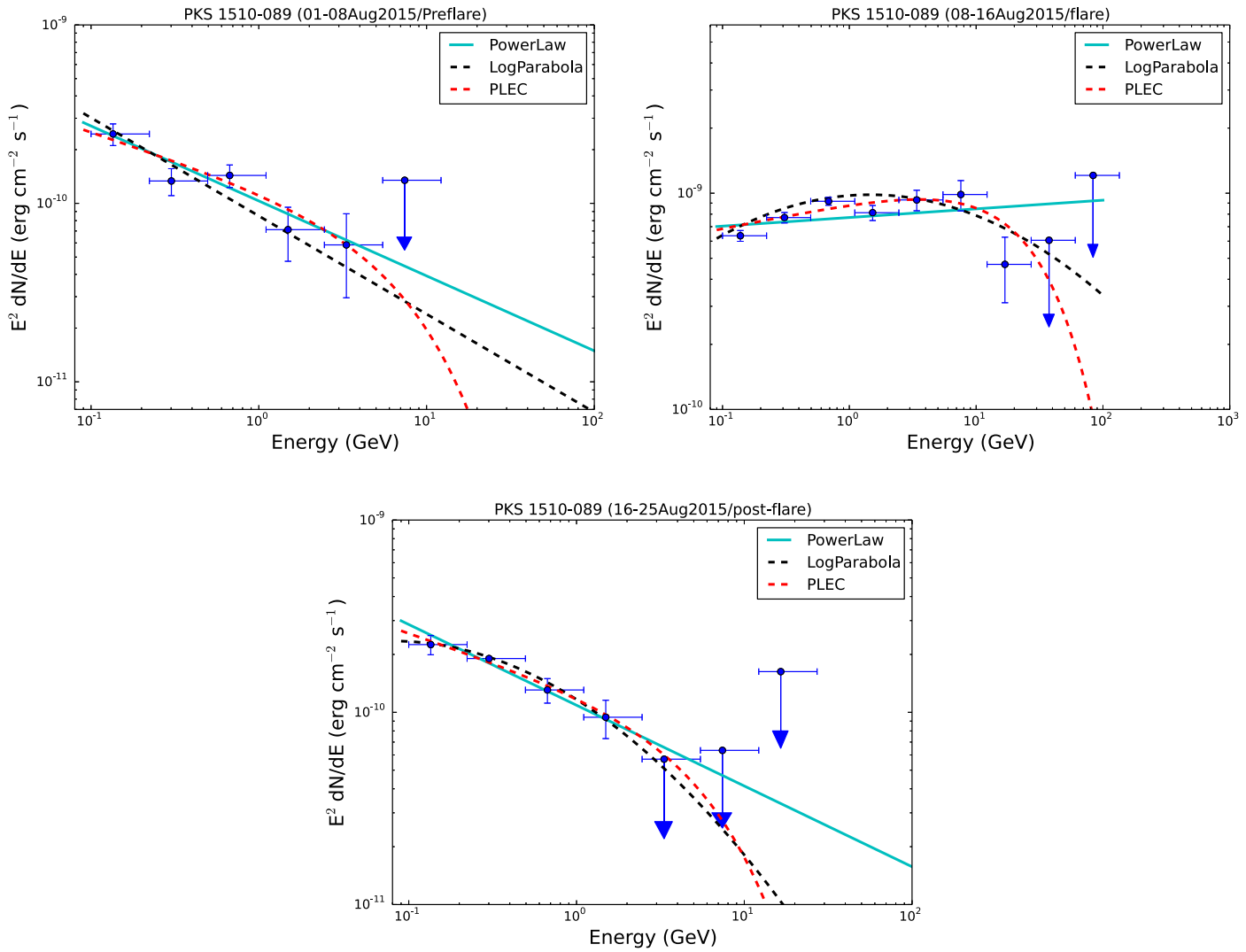

Figure 25. *Fermi*-LAT SEDs during different activity states of flare-4(C) as defined in Figure 12. The PL, LP, and PLEC models are shown in cyan, black, and red, and their respective parameters are given in Table 17.

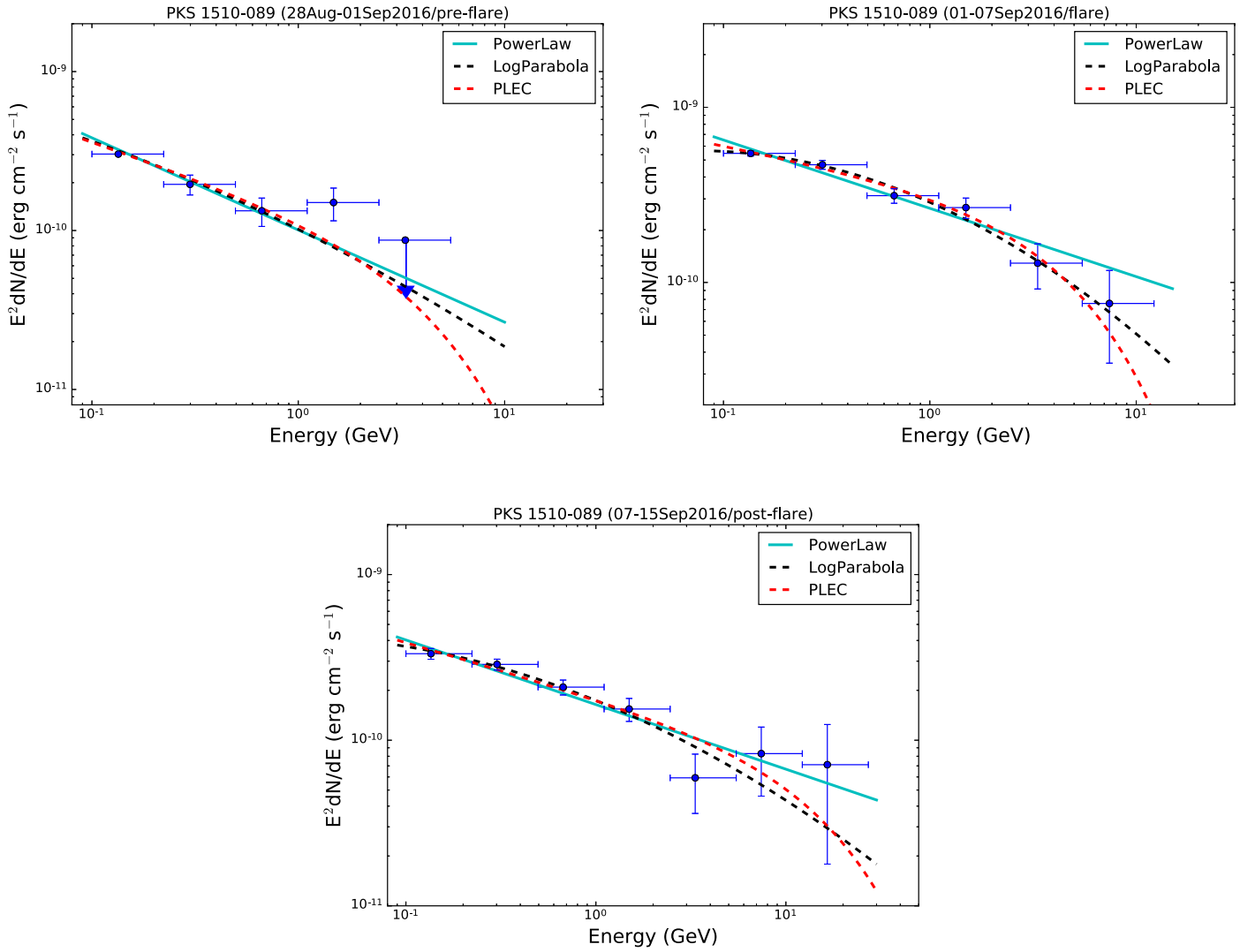

Figure 26. *Fermi*-LAT SEDs during different activity states of flare-5 as defined in Figure 13. The PL, LP, and PLEC models are shown in cyan, black, and red, and their respective parameters are given in Table 18.

Table 19
Reducedχ^2 for SEDs Fitted by Power Law, Log Parabola, and Power Law ExpCutoff for the Flaring Episodes

Activity	Reduced χ^2			$E_{\rm cutoff}$ for PLEC (GeV)
flare-1(A)	PL	LP	PLEC	
flare(I)	2.28	2.31	1.98	30.00 ± 0.25
flare(II)	2.90	0.12	1.09	15.98 ± 6.36
flare-1(B)				
flare	5.06	0.58	1.03	5.74 ± 1.83
flare-2(A)				
flare(I)	3.66	1.91	2.40	11.27 ± 8.13
flare(II)	2.84	0.92	0.48	2.70 ± 0.73
flare-2(B)				
flare	2.15	0.23	0.43	5.82 ± 2.36
flare-2(C)				
flare	1.73	0.41	0.83	18.03 ± 7.53
flare-2(D)				
flare	8.14	0.43	2.83	12.31 ± 3.51
flare-2(E)				
flare(I)	10.23	1.63	2.41	7.61 ± 1.53
flare(II)	0.43	0.15	0.06	9.71 ± 5.12
Flare-3				
flare(I)	2.73	0.91	1.19	5.02 ± 0.18
flare(II)	0.41	0.42	0.34	9.04 ± 0.22
flare-4(A)				
flare	11.93	3.25	5.82	12.78 ± 8.11
flare-4(B)				
flare(I)	2.41	2.95	1.78	9.07 ± 0.31
flare(II)	8.60	0.50	3.30	9.74 ± 3.16
flare-4(C)				
flare	4.41	1.00	1.84	29.71 ± 8.16
Flare-5				
flare	1.55	0.43	0.50	5.01 ± 2.00

Notes. In most cases, LP and in a few cases PLEC provide the best fit to the data. Cutoff energies found with PLEC vary from one flare to another, which could be due to different emission regions of these flares.

3. Results and Discussion

Being from one of the most variable blazars in the Third Source Fermi Catalog (3FGL), the light curve of PKS 1510-089 comprises five major flares, and each flare comprises several subflares. Almost all of the subflares show various phases (pre-flare, flare, plateau, and post-flare), and the flaring phases consist of peaks of different heights. Decay and rising times have been calculated for the major and clear peaks (P1, P2, P3, and so on). Most of the peaks have rising and decay times of a few hours (less than a day). The SEDs of all the phases are fitted with PL, LP, and PLEC functions; the reduced-chiquare and the cut-off energy are mentioned in Table 19.

The brightest flare was observed during 2011 October at MJD 55853.813. For 3 hr binning, the flux was $F_{\rm GeV} = 25.50 \pm 2.34$ with TS = 1340. A new flare was found in 2015 August (Figure 12) that has a peak P1 at MJD 57244.56 with a flux $F_{\rm GeV} = 8.92 \pm 1.25$ (TS = 397.18). More recently, a flare was also observed during 2016 August 28 to September 15 with a flux of $F_{\rm GeV} = 3.15 \pm 0.47$ at MJD 57634.61.

Our results show in detail the presence of subflares within the flares, which we have scanned separately by using the

Table 20
Details of Fastest Variability Timescale of PKS 1510-089 for the Whole Eight Years of Data

$T_{start}(t_1)$ (MJD)	$T_{stop}(t_2)$ (MJD)	Flux Start (F_1) (10^{-6} ph cm^{-2} s^{-1})	Flux Stop (F_2) (10^{-6} ph cm^{-2} s^{-1})	t_{var}(hr)	Δt_{var}(hr)	Rise/Decay
			flare-1(A)			
54916.563	54916.688	1.95 ± 0.45	4.25 ± 0.59	2.67 ± 0.32	1.96 ± 0.17	R
54917.188	54917.313	4.55 ± 0.68	1.75 ± 0.43	−2.18 ± 0.22	−1.60 ± 0.12	D
54917.938	54918.063	0.69 ± 0.25	1.40 ± 0.43	2.96 ± 0.23	2.17 ± 0.12	R
			flare-1(B)			
54945.438	54945.563	0.72 ± 0.29	3.09 ± 0.53	1.43 ± 0.22	1.05 ± 0.12	R
54948.938	54949.063	2.25 ± 0.68	5.49 ± 1.91	2.34 ± 0.12	1.72 ± 0.07	R
54949.688	54949.813	3.10 ± 0.55	1.37 ± 0.36	−2.56 ± 0.26	−1.88 ± 0.14	D
			flare-2(A)			
55739.313	55739.438	0.89 ± 0.36	2.31 ± 0.52	2.17 ± 0.42	1.59 ± 0.22	R
55745.563	55745.688	3.03 ± 0.63	0.95 ± 0.32	−1.79 ± 0.20	−1.32 ± 0.11	D
55745.688	55745.813	0.95 ± 0.32	1.87 ± 0.70	3.07 ± 0.15	2.26 ± 0.08	R
55746.063	55746.188	6.10 ± 1.50	2.95 ± 0.66	−2.88 ± 0.09	−2.12 ± 0.05	D
55746.438	55746.563	7.01 ± 0.95	3.48 ± 0.66	−2.98 ± 0.23	−2.19 ± 0.12	D
55746.563	55746.688	3.48 ± 0.66	1.19 ± 0.43	−1.94 ± 0.31	−1.42 ± 0.17	D
			flare-2(B)			
55767.063	55767.188	1.11 ± 0.45	2.98 ± 0.62	2.11 ± 0.42	1.55 ± 0.23	R
55767.813	55767.938	4.35 ± 1.15	1.94 ± 0.60	−2.59 ± 0.14	−1.90 ± 0.08	D
			flare-2(C)			
55852.063	55852.188	5.80 ± 0.84	1.17 ± 0.43	−1.30 ± 0.18	−0.95 ± 0.10	D
55852.313	55852.438	0.91 ± 0.37	2.57 ± 0.87	2.00 ± 0.13	1.47 ± 0.07	R
55852.438	55852.563	2.57 ± 0.87	5.84 ± 1.75	2.53 ± 0.13	1.86 ± 0.07	R
55853.063	55853.188	3.11 ± 0.65	6.28 ± 0.87	2.97 ± 0.30	2.18 ± 0.16	R
55853.188	55853.313	6.28 ± 0.87	3.00 ± 0.60	−2.81 ± 0.24	−2.07 ± 0.13	D
55853.563	55853.688	3.46 ± 1.43	7.20 ± 2.54	2.84 ± 0.24	2.09 ± 0.13	R
55853.688	55853.813	7.20 ± 2.54	25.50 ± 2.34	1.64 ± 0.34	1.21 ± 0.18	R
55853.938	55854.063	13.35 ± 1.27	4.94 ± 0.76	−2.09 ± 0.12	−1.54 ± 0.07	D
			flare-2(D)			
55867.313	55867.438	3.49 ± 0.70	1.38 ± 0.59	−2.24 ± 0.54	−1.64 ± 0.29	D
55868.438	55868.563	6.92 ± 1.09	2.74 ± 1.15	−2.25 ± 0.64	−1.65 ± 0.35	D
55868.688	55868.813	1.62 ± 0.72	3.55 ± 0.74	2.66 ± 0.81	1.95 ± 0.43	R
55869.063	55869.188	4.78 ± 0.81	2.19 ± 0.52	−2.67 ± 0.24	−1.96 ± 0.13	D
55869.188	55869.313	2.19 ± 0.52	4.50 ± 0.77	2.89 ± 0.27	2.12 ± 0.15	R
55870.313	55870.438	2.05 ± 0.58	4.10 ± 0.90	3.00 ± 0.28	2.20 ± 0.15	R
55872.563	55872.688	2.66 ± 0.87	6.11 ± 0.86	2.50 ± 0.56	1.84 ± 0.30	R
			flare-2(E)			
55989.188	55989.313	3.54 ± 0.59	1.15 ± 0.39	−1.84 ± 0.28	−1.35 ± 0.15	D
55989.313	55989.438	1.15 ± 0.39	2.77 ± 0.56	2.36 ± 0.36	1.74 ± 0.20	R
55990.063	55990.188	1.35 ± 0.38	2.67 ± 0.53	3.06 ± 0.36	2.25 ± 0.20	R
55990.438	55990.563	1.94 ± 0.54	4.33 ± 0.78	2.59 ± 0.32	1.90 ± 0.17	R
55991.313	55991.438	1.01 ± 0.43	2.07 ± 0.50	2.89 ± 0.73	2.12 ± 0.40	R
55991.813	55991.938	1.82 ± 0.43	0.84 ± 0.32	−2.68 ± 0.50	−1.97 ± 0.27	D
55998.938	55999.063	0.78 ± 0.30	1.80 ± 0.54	2.49 ± 0.26	1.83 ± 0.14	R
56000.188	56000.313	1.25 ± 0.41	0.63 ± 0.27	−3.04 ± 0.44	−2.23 ± 0.24	D
56000.688	56000.813	1.35 ± 0.37	2.75 ± 0.52	2.94 ± 0.35	2.16 ± 0.19	R
56001.063	56001.188	2.12 ± 0.45	1.07 ± 0.39	−3.03 ± 0.61	−2.23 ± 0.33	D
			flare-3			
56556.188	56556.313	1.61 ± 0.49	3.88 ± 0.66	2.37 ± 0.36	1.74 ± 0.19	R
56563.313	56563.438	2.05 ± 0.52	0.93 ± 0.39	−1.98 ± 0.38	−1.45 ± 0.21	D
56568.063	56568.188	2.10 ± 0.49	0.99 ± 0.35	−2.76 ± 0.53	−2.03 ± 0.29	D
			flare-4(A)			
57113.188	57113.313	0.30 ± 0.13	0.93 ± 0.33	1.84 ± 0.15	1.35 ± 0.08	R
57116.938	57117.063	3.65 ± 0.49	1.73 ± 0.42	−2.78 ± 0.40	−2.04 ± 0.22	D

Table 20
(Continued)

$T_{start}(t_1)$ (MJD)	$T_{stop}(t_2)$ (MJD)	Flux Start (F_1) (10^{-6} ph cm^{-2} s^{-1})	Flux Stop (F_2) (10^{-6} ph cm^{-2} s^{-1})	t_{var}(hr)	Δt_{var}(hr)	Rise/Decay
			flare-4(B)			
57164.063	57164.188	1.40 ± 0.38	0.63 ± 0.29	−2.61 ± 0.62	−1.92 ± 0.34	D
57165.688	57165.813	0.97 ± 0.34	2.06 ± 0.47	2.78 ± 0.44	2.04 ± -0.24	R
57166.188	57166.313	1.30 ± 0.46	2.85 ± 0.61	2.66 ± 0.48	1.95 ± 0.26	R
57166.438	57166.563	2.43 ± 0.51	0.98 ± 0.36	−2.29 ± 0.40	−1.68 ± 0.21	D
57166.688	57166.813	1.27 ± 0.41	3.05 ± 0.67	2.38 ± 0.29	1.75 ± 0.16	R
57169.688	57169.813	1.15 ± 0.40	2.21 ± 0.52	3.19 ± 0.58	2.34 ± 0.31	R
57170.438	57170.563	3.61 ± 0.69	0.81 ± 0.34	−1.39 ± 0.21	−1.02 ± 0.11	D
			flare-4(C)			
57243.438	57243.563	0.57 ± 0.25	1.98 ± 0.60	1.67 ± 0.19	1.23 ± 0.10	R
57245.813	57245.938	4.60 ± 1.55	2.37 ± 0.94	−3.14 ± 0.29	−2.31 ± 0.16	D
57249.563	57249.688	0.78 ± 0.32	1.94 ± 0.66	2.27 ± 0.18	1.67 ± 0.10	R
			flare-5			
57632.563	57632.688	1.03 ± 0.37	2.09 ± 0.54	2.00 ± 0.33	1.47 ± 0.18	R
57634.938	57635.063	2.30 ± 0.50	1.06 ± 0.35	−2.68 ± 0.39	−1.97 ± 0.21	D
57635.063	57635.188	1.06 ± 0.35	2.13 ± 0.49	2.98 ± 0.43	2.19 ± 0.23	R
57635.188	57635.313	2.13 ± 0.49	0.80 ± 0.30	−2.12 ± 0.31	−1.56 ± 0.17	D

Notes. Data that have a significance of at least 5σ have been considered (see the text for details). Here t_{var} represents the observed characteristic timescale, and $\Delta t_{var} = t_{var}\,(1+z)^{-1}$. The parameters R (rise) and D (decay) represent the behavior of the flux in a particular time interval.

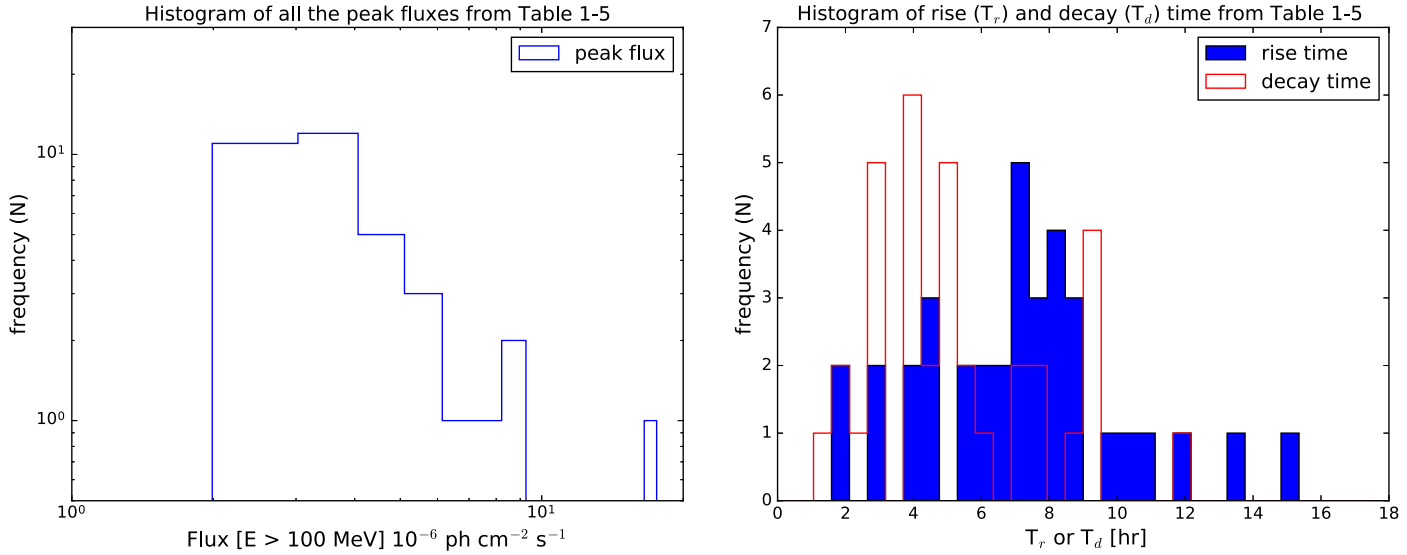

Figure 27. Left panel: histogram of peak fluxes from Tables 1–5. The mean flux is 3.54 ± 0.08, and the standard deviation of the sample is 1.69. Right panel: histogram of rise and decay times from Tables 1–5. Their mean values are 6.04 ± 0.22 hr and 3.88 ± 0.16 hr, respectively. The sample standard deviations are 2.40 hr and 2.20 hr.

following function,

$$F(t_2) = F(t_1).2^{(t_2-t_1)/t_d}, \quad (5)$$

to calculate the minimum time of doubling or halving of the flux between the time instants t_1 and t_2; $F(t_1)$ and $F(t_2)$ are respectively the fluxes measured at t_1 and t_2; and t_d represents the doubling/halving timescale. The results are shown in Table 20 for the 3 hr bin of the light curve. While scanning the light curve, the following criteria were used: the flux should be double/half between two consecutive time instants, and for these instants of time the condition TS > 25 ($\sim 5\sigma$ detection) must be satisfied. From Table 20, we find that the shortest observed variability time for the rising part is $t_{rise} = 1.43 \pm 0.22$ hr between MJD 54945.438 and 54945.563 (flare-1(B)), and for the decaying part $t_{decay} = 1.30 \pm 0.18$ hr between MJD 55852.063 and 55852.188 (flare-2(C)). There were also some other time intervals within which the flux changed by a factor of 2, but they did not satisfy the requirement of TS > 25. Such time intervals are ignored in our analysis to find the fastest variability timescale. The

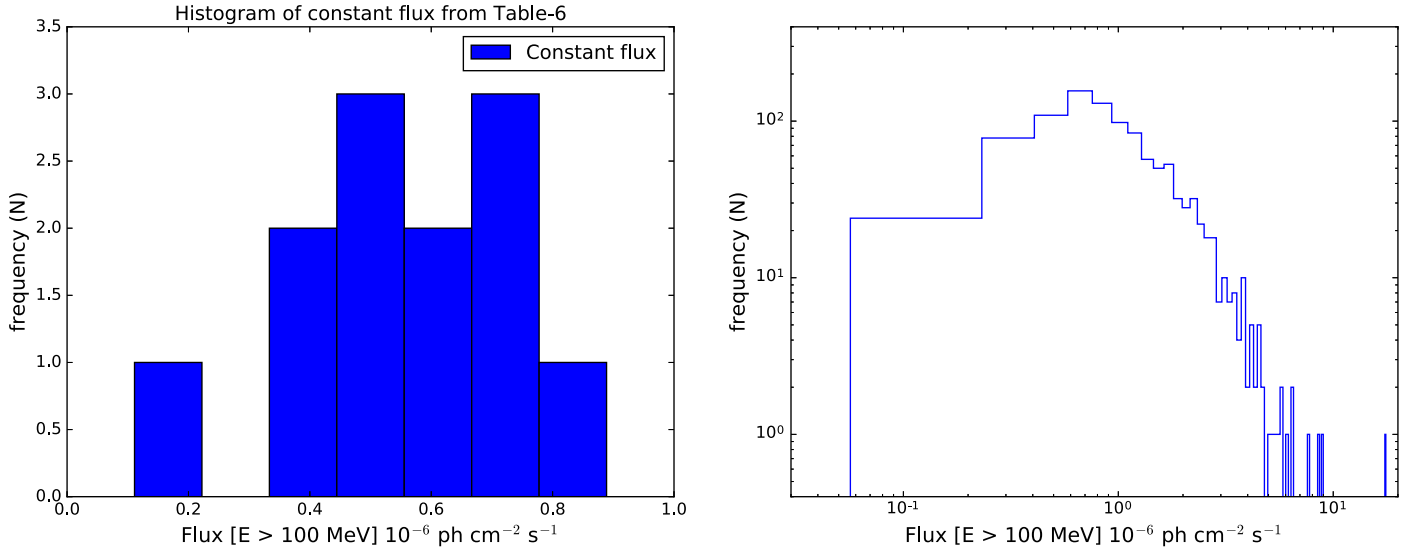

Figure 28. Left panel: histogram of constant flux from Table 6. The mean constant flux is found to be 0.51 ± 0.01, and the standard deviation is 0.20. Right panel: histogram of all of the flux data points. The distribution is peaked, with a slow rise up to the peak and a fast decay after that.

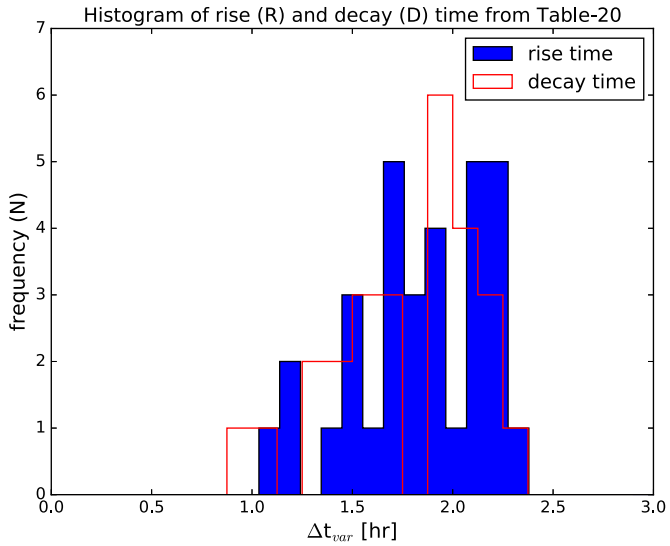

Figure 29. Histogram of the rise and decay times from the fastest variability time, Table 20. They are distributed with means of 1.75 ± 0.02 hr and 1.76 ± 0.02 hr and standard deviations of 0.35 hr and 0.40 hr, respectively.

hour-scale variability time was also found earlier by Brown (2013) and Saito et al. (2013) for PKS 1510-089. The variability time (the fastest halving/doubling time t_d is the fastest variability time $t_{\rm var}$) gives an idea about the size of the emission region if we know the Doppler factor δ for the source. The variability time $t_{\rm var}$, the size of the emission region R, and the Doppler factor δ are related by

$$R \leqslant c t_{\rm var} \delta (1+z)^{-1} \quad (6)$$

where z is the redshift of the source. The redshift-corrected variability time ($\Delta t_{\rm var} = t_{\rm var}(1+z)^{-1}$) is used to calculate the size of the emission region while modeling the SEDs of blazars. The apparent speed in the ultrarelativistic jet of PKS 1510-089 has been observed to be up to 46c(Jorstad et al. 2005), which suggests that the Doppler factor could be very high for this source. From Equation (6) for $t_{\rm var} = 1.30$ hr, $\delta = 47$ (Kadota et al. 2012), we get an emission region of radius $R \sim 4.85 \times 10^{15}$ cm. A less extreme Doppler factor of 10 would imply an emission region of radius $R \sim 1.03 \times 10^{15}$ cm. This is comparable to the estimates by Brown (2013) and Saito et al. (2013), which are $\sim 9.3 \times 10^{15}$ cm and $\sim 1.5 \times 10^{15}$ cm, respectively. Such small emission regions are rather difficult to accommodate in the standard framework where the emission takes place at a large distance from the central engine (see Tavecchio et al. 2010 and references therein for a more detailed discussion).

A multiwavelength study of Flare-1 (2009 March–April) has been done by Abdo et al. (2010a). They found that the γ-ray flux had no correlation with the X-ray flux, but it showed significant correlation with the optical flux. They also found that the optical flux was lagging 13 days behind the γ-ray flux. Moreover, they estimated the isotropic luminosity above 100 MeV during flare(II) of flare-1(A) to be more than 2×10^{48} erg s^{-1}. The same flare has also been observed by HESS (Abramowski et al. 2013) in very high energy gamma rays. According to their estimate, the integral flux in the very high energy (0.15–1.0 TeV) band is $1.0 \pm 0.2_{\rm stat} \pm 0.2_{\rm sys} \times 10^{-11}$ cm^{-2} s^{-1} , which is ≈3% of the integral flux from the Crab Nebula. It also shows the steepening in the photon spectrum with spectral index $5.4 \pm 0.7_{\rm stat} \pm 0.3_{\rm sys}$ for the PL distribution. Foschini et al. (2013) have studied the outburst of 2011 October–November. They estimated the shortest variability time ever detected in the MeV–GeV energy regime as ∼20 minutes at MJD 55852 by using the GTI time binning. They also mentioned the hour-scale variability (see Table 1 of Foschini et al. 2013) by using the 3 hr time binning, which is consistent with the result of Brown (2013) and Saito et al. (2013). We note that our result shows that the shortest variability time is ∼1.30 hr (by using 3 hr binning) between MJD 55852.063 and 55852.188.

A multiwavelength study of Flare-2(E) was also done by the MAGIC collaboration (Aleksić et al. 2014). They used the data from *Fermi*-LAT observations during 2012 January 1 to April 7 (MJD 55927–56024). Within the time interval MJD 55974 to

55994, they estimated the shortest variability timescale as $t_{\rm var} = 1.5 \pm 0.6$ hr, which is very close to the value we estimated, $t_{\rm var} = 1.84 \pm 0.28$ hr (for almost the same time interval), given in Table 20 (flare-2E).

Flare-3 has never been studied in the past. The maximum flux of this flare was found to be around $F_{\rm GeV} = 3.47 \pm 0.47$ at MJD 56554.1 in our study. The fastest variability time for this flare was estimated as $t_{\rm var} = 1.98 \pm 0.38$ hr (Table 20, Flare-3), which is comparable to the fastest variability time found for other flares.

We have also presented a detailed study of flare-4(A) (MJD 57100–57128) and flare-4(C) (MJD 57235–57259) for the first time, where flare-4(C) was identified as the third brightest flare in the history of PKS 1510-089. The MAGIC collaboration (Ahnen et al. 2017) previously performed a multiwavelength study of flare-4(B) observed in May 2015 (MJD 57143–57177).

Flare-5 was found to be a very recent flare of PKS 1510-089. The shortest variability time was calculated as $t_{\rm var} = 2.00 \pm 0.33$ hr (Table 20).

Figure 27 shows the histogram of the peak fluxes and the rise and decay times of the peak fluxes, as also enumerated in Tables 1–5. The rise and decay times for the different peaks of the flares are distributed around a mean of 6.04 ± 0.22 hr and 3.88 ± 0.16 hr with a standard deviation of 2.40 hr and 2.20 hr, respectively, while the peak fluxes are distributed around a mean of 3.54 ± 0.08 with a standard deviation of 1.69. Histograms of the constant fluxes are plotted in Figure 28. They are distributed with a mean of 0.51 ± 0.01 and standard deviation of 0.20, which implies that the quiescent state of the source is pretty stable. A frequency distribution of all the flux data points is also plotted in the right-hand panel of Figure 28. The plot shows a peaked distribution with a slowly rising part up to the peak and a fast-decaying part beyond the peak. The peak value signifies the flux where the source spends most of the time. Above the peak, the flux values fall rapidly along with a few outliers that can be associated with large flux variations in the source. Tavecchio et al. (2010) have studied flux variations and duty cycles with 1.5 years of data in two of the most variable sources, PKS 1510-089 and 3C 454.3. Our findings with a much larger data set also show a behavior very similar to their study.

In Figure 29, we have plotted the histogram of redshift-corrected variability time $\Delta t_{\rm var}$ (see Table 20). One can clearly see that the distributions for rise and decay are not Gaussian, but the data points are distributed with means of 1.75 ± 0.02 hr and 1.76 ± 0.02 hr and with standard deviations of 0.35 hr and 0.40 hr, respectively.

Figure 14 shows the variation of photon index as a function of integral fluxes for a few subflares. These plots reveal that when the source gets brighter, its photon spectrum gets harder, a feature which has also been seen in many other blazars. A similar result was also reported earlier (see Foschini et al. 2013).

We obtained the SEDs for different phases (pre-flare, plateau, flare, and post-flare) and fitted them with different functional forms (differential photon spectrum following PL, LP, and PLEC distributions). To get the best fit, we calculated the Δlog(likelihood) and reduced χ^2 for each phase.

We compared the reduced χ^2 values for the PL, LP, and PLEC fits and the spectral cutoff energies in Table 19 for different flares. In almost all of the cases, the best fit is found to be LP during flaring episodes. We also note that in the case of the PLEC fit, the spectral cutoff energy varies from one flare to another. It is interesting to note that in a few cases where the reduced chi-squared values for PLEC are comparable to the values obtained from LP fits, the cutoff energy is well constrained. This has strong physics implications regarding the location of the emission region. If the emission region is close to the core of the source, pair-production optical depth would prevent the escape of very high energy gamma rays. As a result, the highest energy gamma rays are expected from zones outside the BLR region, in the optically thin outer jet region (see Aleksić et al. 2014, MAGIC Collaboration). The variations in spectral fittings and spectral cutoff energies of the flares indicate that different flares might have originated from different zones along the length of the jet of PKS 1510-089. Earlier studies on blazar flares also indicated the possibility of multiple zones of emission during flares (Dotson et al. 2012, 2015; Brown 2013). Detailed broadband spectral modeling with photon data ranging from radio to TeV energy would be more useful in exploring the complex nature of flares of this highly variable source.

4. Concluding Remarks

We have studied the long-term light curve of PKS 1510-089 with the data collected by *Fermi*-LAT between 2008 August and 2016 December. The data have been binned in 7 days, 1 day, and 6 hr periods to explore various features of the light curve. Five major flares along with many substructures have been detected in the weekly binning of the data and have been further studied in detail. From a detailed study on variability, the shortest variability time has been found to be close to 1 hr. This puts a strong constraint on the size of the emission region, which has been estimated to be $\sim 10^{15}$ cm for reasonable values of the Doppler factor. The SEDs have been fitted with three different functional forms: PL, LP, and PLEC. We find that in the majority of the flares, LP gives the best fit, and in some cases PLEC can reasonably describe the data. Moreover, when PLEC gives the best fit, the cutoff energies are found to vary from one flare to another. Our results indicate that the emission regions vary from one flare to another, which is consistent with earlier results.

We thank the referee for insightful comments that improved our work significantly. It is also our pleasure to thank R. J. Britto and V. S. Paliya for many fruitful and helpful discussions on the topic. This work has made use of public *Fermi* data obtained from the Fermi Science Support Center (FSSC), provided by NASA Goddard Space Flight Center.

References

Abdo, A. A., Ackermann, M., Agudo, I., et al. 2010a, ApJ, 721, 1425
Abdo, A. A., Ackermann, M., Ajello, M., et al. 2010b, ApJ, 722, 520
Abramowski, A., Acero, F., H.E.S.S. Collaboration, et al. 2013, A&A, 554, A107
Acero, F., Ackermann, M., Ajello, M., et al. 2015, ApJS, 218, 23
Ahnen, M. L., Ansoldi, S., MAGIC Collaboration, et al. 2017, A&A, 603, A29
Albert, J., Aliu, E., Anderhub, H., et al. 2007, ApJ, 669, 862
Aleksić, J., Ansoldi, S., Antonelli, L. A., et al. 2014, A&A, 569, A46
Atwood, W. B., Abdo, A. A., Ackermann, M., et al. 2009, ApJ, 697, 1071
Barnacka, A., Moderski, R., Behera, B., Brun, P., & Wagner, S. 2014, A&A, 567, A113
Böttcher, M., & Dermer, C. D. 1998, ApJL, 501, L51
Böttcher, M., Reimer, A., Sweeney, K., & Prakash, A. 2013, ApJ, 768, 54
Britto, R. J., Bottacini, E., Lott, B., Razzaque, S., & Buson, S. 2016, ApJ, 830, 162

Brown, A. M. 2013, MNRAS, 431, 824
Burbidge, E. M., & Kinman, T. D. 1966, ApJ, 145, 654
Dotson, A., Georganopoulos, M., Kazanas, D., & Perlman, E. S. 2012, ApJL, 758, L15
Dotson, A., Georganopoulos, M., Meyer, E. T., & McCann, K. 2015, ApJ, 809, 164
Foschini, L., Bonnoli, G., Ghisellini, G., et al. 2013, A&A, 555, A138
Jorstad, S. G., Marscher, A. P., Lister, M. L., et al. 2005, AJ, 130, 1418
Kadota, A., Fujisawa, K., Sawada-Satoh, S., Wajima, K., & Doi, A. 2012, PASJ, 64, 109
Kelly, B. C., Sobolewska, M., & Siemiginowska, A. 2011, ApJ, 730, 52
Mattox, J. R., Bertsch, D. L., Chiang, J., et al. 1996, ApJ, 461, 396
Paliya, V. S. 2015, ApJL, 808, L48
Pratim Basumallick, P., & Gupta, N. 2017, APh, 88, 1
Saito, S., Stawarz, Ł., Tanaka, Y. T., et al. 2013, ApJL, 766, L11
Spada, M., Ghisellini, G., Lazzati, D., & Celotti, A. 2001, MNRAS, 325, 1559
Tavecchio, F., & Ghisellini, G. 2008, MNRAS, 386, 945
Tavecchio, F., Ghisellini, G., Bonnoli, G., & Ghirlanda, G. 2010, MNRAS, 405, L94
Thompson, D. J., Djorgovski, S., & de Carvalho, R. 1990, PASP, 102, 1235
Zacharias, M., Böttcher, M., Chakraborty, N., et al. 2016, arXiv:1611.02098